BANDWIDTH ENHANCEMENT AND MINIATURIZATION TECHNIQUES FOR SMALL ANTENNAS

by

Ting-Yen Shih

A dissertation submitted in partial fulfillment of
the requirements for the degree of

Doctor of Philosophy

(Electrical and Computer Engineering)

at the

UNIVERSITY OF WISCONSIN–MADISON

2017

Date of final oral examination: 5/10/2017

The dissertation is approved by the following members of the Final Oral Committee:

Nader Behdad, Professor, Electrical and Computer Engineering
Zhenqiang Ma, Professor, Electrical and Computer Engineering
Irena Knezevic, Professor, Electrical and Computer Engineering
Mikhail Kats, Assistant Professor, Electrical and Computer Engineering
Peter Timbie, Professor, Physics

This dissertation is dedicated to my family,

Tschen-wei Chang,

Kuo-Hsiung Shih,

Su-Li Hsu,

San-Lii Chang,

Lien-Chuan Yeh,

and Yi-Lun Shih.

ACKNOWLEDGMENTS

I would like to gratefully acknowledge the guidance, support and encouragement of my doctoral advisor, Dr. Nader Behdad, and the members of my committee, Dr. Zhenqiang Ma, Dr. Irena Knezevic, Dr. Mikhail Kats, and Dr. Peter Timbie, during my time at the University of Wisconsin-Madison, as well as Dr. Zongfu Yu for his support.

My gratitude extends to my friends and labmates at the University of Wisconsin-Madison for all the insightful discussions and help.

This dissertation would not have been possible without funding from the Office of Naval Research under ONR Awards No. N00014-11-1-0618, N00014-15-1-2207, and N00014-16-1-2098.

Finally, I would like to thank my family for their love and support. Special thanks to my wife, Tschen-wei Chang, for supporting me in my life, research, and career, and also for her constant encouragement over the years. I couldn't have achieved what I have achieved without her.

DISCARD THIS PAGE

TABLE OF CONTENTS

Page

DISCARD THIS PAGE

LIST OF TABLES

DISCARD THIS PAGE

LIST OF FIGURES

Figure Page

Appendix
Figure Page

Appendix
Figure Page

Appendix
Figure Page

ABSTRACT

The HF/VHF frequency bands (3-300 MHz) are used by various long-range wireless communication systems in both military and commercial applications. Due to the large wavelengths in these bands, the antennas used in such applications are often electrically-small. While wide bandwidth is desired for high data rates, the electrically-small antennas (ESAs) tend to have very small bandwidth since there is a trade-off between small antenna size and wide bandwidth. For each ESA, the upper bound of its bandwidth can be calculated. Despite the fact that fundamental limitations restrain the performance of small antennas, the growing need of compact and broadband wireless devices for communication and sensor systems has tremendously stimulated the demand for small antennas with performance levels approaching, or even exceeding, these limitations. To address this need, I pursue novel bandwidth enhancement and miniaturization techniques for small antennas.

In this dissertation, three parallel approaches that I took to investigate bandwidth enhancement and miniaturization techniques for small antennas are presented. The first method employs a novel loading structure to allow antennas to achieve compact and miniaturized dimensions while maintaining a wide bandwidth. The second method involves utilizing the presence of metallic objects that are in the vicinity of the ESAs–more specifically, the platforms (e.g. vehicles, airplanes) on which the ESAs are mounted. In this method, the platforms are considered as the main radiators, and the ESAs act mainly as coupling

elements. The third method is to design highly-efficient active non-Foster matching circuits to bypass the gain-bandwidth limitations of the ESAs and achieve wide impedance bandwidth. All three methods have been experimentally validated.

Chapter 1

Introduction

1.1 Motivation

Antennas, the transitional structures between free-space and a guiding device that transmit or receive electromagnetic waves, played a vital role in the success of wireless communication. Bandwidth enhancement and miniaturization techniques of antennas have been discussed as two of the most interesting subjects in the antenna design field. Todays needs for more multi-functional systems impose requirements for small mobile terminals including mobile phones, radio frequency identification (RFID), wireless power transmission, etc. In these multi-functional systems and in many other applications, such as high frequency/very high frequency (HF/VHF) communications and amplitude modulation (AM) broadcasting, antennas are electrically small, i.e. the size of the antennas is much smaller than a wavelength at the operational frequency. Small antennas have been widely studied since 1947 [1]. Numerous research groups studying the relationship between the electrical dimensions of an antenna and its gain [2–8], radiation efficiency, bandwidth [1, 2, 5, 7, 9–11], and directional characteristics [2–4, 6, 12–17] have pointed to a set of physical bounds that restrain the performance of small antennas. The performance of such small antennas are often characterized by their sizes, their quality factors, their fractional bandwidth, and their gain. Therefore, it is important to understand these parameters.

The product of the parameter ka is commonly used to evaluate the electrical size of an antenna. Where k is the wave number ($2\pi/\lambda$, where λ is the wavelength), and a is the radius of the minimum size sphere that encloses the antenna. When $ka < 1$, an antenna is considered electrically small [5]. The quality factor Q, is a dimensionless parameter that characterizes bandwidth of a resonator or an antenna relative to its resonant frequency [2, 18]. The lower bound of the Q of a small antenna with a given size is of particular interest because it is inversely proportional to the maximum available antenna bandwidth

(approximately). At any fixed minimum Q, a trade-off exists between the antenna size and the maximum available bandwidth. In particular, as the dimensions of an antenna are decreased, its bandwidth also decreases with an upper bound that can be derived by its minimum Q. For example, at 10 MHz, the upper bound for the matched impedance bandwidth of a dipole antenna with a maximum dimension of 1 m can be calculated from [2, 19] to be less than 0.1% (or 10 kHz). This is very narrowband.

Despite the fact that fundamental limitations restrain the performance of small antennas [1–7, 9–11], the growing need of compact and broadband wireless devices for communication and sensor systems that use the electromagnetic spectrum has tremendously stimulated the demand for small antennas with performance levels approaching, or even exceeding, these limitations. To address this need, we propose to investigate novel bandwidth enhancement and miniaturization techniques for electrically-small antennas (ESAs).

1.2 Proposed Approach

We pursue three parallel approaches to investigate bandwidth enhancement and miniaturization techniques for small antennas. These are:

1. Improving the antenna structure,
2. Utilizing the platform, and
3. Using non-Foster matching circuits.

Improving the antenna structure is the most direct way to miniaturize an antenna. Some well-known antenna miniaturization techniques include shaping the antenna, loading materials, and using electromagnetic metamaterials [20]. ESAs designed using these conventional miniaturization techniques, however, generally suffer from bandwidth reduction. We designed a low-profile, compact spiral antenna with a broadband circularly polarized

response using a novel loading structure which possesses both inductive and capacitive characteristics. The proposed antenna occupies a volume that is 89% smaller than that occupied by its conventional counterpart.

Utilizing other structures in the vicinity of the ESA is another way to enhance bandwidth. Realization methods include placing the antenna on a large ground plane, using highly-conductive ground planes, and taking advantage of the platform where the antennas are mounted. Our second approach focuses on taking advantage of the platform. In many applications, the antennas are mounted on physically-large metallic platforms, such as ships, vehicles, airplanes, etc. Since these platforms are generally larger than the antenna mounted on it, if the platform can be used as the main part of the radiating structure, the maximum linear dimension of the main radiator can be increased and the bandwidth problems can be alleviated. We proposed a systematic method for designing antenna systems that takes advantage of the presence of the platform to achieve significantly enhanced bandwidth compared to a stand-alone antenna. This enhanced bandwidth is achieved despite the fact that the maximum linear dimensions of the antenna system (i.e. the antenna(s) and the platform) are not changed.

Our third approach employs external non-Foster matching circuits. The reactance of an ESA increases with decreasing electrical dimensions [1]. For these antennas, the effectiveness of passive matching is severely limited, as imposed by the gain-bandwidth theory of Bode, Fano, and Youla [21–23]. Non-Foster matching circuits produce negative inductance or capacitance that allow for bypassing the restrictions of the gain-bandwidth theory, and for achieving wide bandwidth. However, the use of conventional non-Foster matching circuits often sacrifices the transmission efficiency or the stability of the antenna system. We proposed a new non-Foster matching network for electrically-small monopole antennas in transmit applications which achieves wide bandwidth, high transmission efficiency, and stability at the same time.

1.3 Literature Review

Despite the significant amount of research in the area, the design problems of ESAs with wide bandwidth remain unsolved. It was proven by numerous studies that a set of physical bounds exists that restrains the performance of small antennas [1, 2, 4–7, 9–11]. Wheeler was the first to introduce the definition of ESAs, as well as an equivalent-circuit-model-based method to define the limitations of these antennas [1]. In [2], the concept and the calculation method of the minimum Q of ESAs were established. Chu's Q is considered a more accurate measure of the physical limitations of ESAs than Wheelers. Todays needs for multifunctional wireless systems, however, drive requirements for ESAs with performance levels approaching, or even exceeding, these bandwidth bounds.

The following subsections provide a brief introduction to the research done in the past regarding bandwidth enhancement and miniaturization techniques for ESAs.

1.3.1 Improving the Antenna Structure

Most antennas either demonstrate broadband responses or have compact sizes. However, having both of these criteria in a single antenna is highly desirable in many applications. To address this need, antenna miniaturization techniques that do not sacrifice bandwidth are needed. A promising method to achieve this goal is to start with frequency independent antennas, such as spiral antennas, and to employ size reduction techniques. A number of different spiral antenna miniaturization techniques have been examined in the past [20, 24–30]. These techniques can be categorized into three classes: inductive loading (series inductance), capacitive loading (shunt capacitance), and slow-wave treatments (series inductance and shunt capacitance). Inductive loading increases the inductance per unit length of the spiral arms. Some of the well known realization methods are: using a

series of lumped inductors along spiral arms [28], using two dimensional (2-D) meandering lines [20, 24–26], and using three dimensional (3-D) coils [29]. Similarly, capacitive loading increases the capacitance per unit length of the spiral arms. This can be realized by using dielectric material loading [20] and tapered dielectric loading [27]. The slow-wave treatment is a combination of inductive and capacitive loading. It increases both the series inductance and the shunt capacitance per unit length. In [29], the slow-wave treatment was realized by using 3-D coils in combination with dielectric loading. Small antennas designed using these conventional miniaturization techniques, however, generally suffer from bandwidth reduction.

1.3.2 Utilizing the Platform

Since many antennas are mounted on metallic platforms that are physically larger than the antennas themselves, the presence of the platform in the vicinity of the antenna may be exploited to enhance the antenna bandwidth. To do this, the platform and the antenna must be designed together and the platform must be considered to be a major part of the radiating structure from the beginning. In the past, various research groups have studied platform-mounted antennas and proposed different techniques for taking advantage of the platform. Specifically, in [31–39], the platform-mounted antennas were designed to take advantage of the platform. These platform-mounted antennas can be categorized into two classes: 1) Partially exciting the platform modes [31, 34–38], and 2) Fully exciting the platform modes [39]. In [31], HF fan/whip antennas placed on the superstructure of a ship to excite currents on a portion of the ships structure were discussed. In [34–36], part of the platform was used as the radiator and part of a folded monopole antenna was replaced by the mast of a ship. In [37], the half loop antennas were flush-mounted at the modified ship corners to take advantage of part of the platform as reflecting plane. In a more recent study, a characteristic-mode-based approach was employed to find desirable

radiating currents from the characteristic modes of the platform [38]. To excite the desired currents on the structure, slits were cut in the body of the ship where the currents are strongest. In [39], the theory of characteristic modes was used to determine the optimized positions of the feed probes to excite the radiating currents on a unmanned aerial vehicle (UAV).

1.3.3 Using Non-Foster Circuits

ESAs have very small radiation resistances and large reactances [1]– [19]. Consequently, they have very high radiation Qs, and are difficult to match. When matched with conventional passive circuits composed of positive valued capacitors or inductors (Foster circuits), ESAs suffer from narrow bandwidth or from low gain due to the realizability constraints imposed by the gain-bandwidth limitation theory [21]– [23]. This is because positive valued capacitors or inductors are only capable of canceling out the reactance of an ESA at discrete frequencies. In theory, active non-Foster matching circuits produce lossless impedances with a negative reactance-to-frequency slope that allow for bypassing the gain-bandwidth limitations by canceling out the reactance of the ESA over a wide and continuous frequency band. This technique has been widely used in receiving ESA systems [40]– [44]. In 1968, the earliest application of non-Foster matching circuit to electrically-small receiving antennas was proposed [40]. The multistage transistor-based circuit in this work provides negative capacitance that is controlled by a voltage feedback loop. The advantage of using negative impedance matching circuits for receive ESAs was also stated. It improves received signal-to-noise ratio (SNR) only in those frequency ranges where receivers are internal-noise limited but not external-noise limited. This research was extended in [41] where the negative capacitance is realized using operational amplifiers. In [42], active coupling networks are used for electrically-small receiving antennas, but the inherent bandwidth and noise issues with solid state devices limited their

use. The designs in [43] use transistor-based negative impedance converters (NICs, introduced by [45]) to generate negative capacitors or negative inductors to implement non-Foster circuits for receive antennas. A 9 dB SNR improvement was achieved at 30 MHz in an actual experiment. In [44], it was suggested that, with low-noise floor levels, a receiving system consisting of a passive ESA and an amplifier can provide better SNRs compared with a receiving system with a non-Foster matched ESA. On the other hand, little work has been published on non-Foster matching techniques for ESAs in transmit applications [43, 46]. In the experiments in [46], the use of class A and class B NICs[1] resulted in transducer power gain improvements compared to passive matching circuits that exceeded 20 dB in the lower part of the operating frequency band (15 MHz–30 MHz, 67% transducer power gain improvement bandwidth); while in [43], the class C NIC improved the transducer power gain by 10 dB at the center part of the operating frequency band (21 MHz–22.2 MHz, 6% transducer power gain improvement bandwidth). There are some additional challenges that must be overcome for designing transmit matching circuits for ESAs. First, the matching loss magnification must be overcome. Matching loss magnification reduced the transmission efficiency (low transducer power gain) between the source and the antenna because of the multiple reflections[2] that exist between a high Q ESA and its matching circuit [47]. Secondly, a non-Foster transmit antenna must be capable of handling very high voltage/current swings at the antenna terminals to allow for sufficient power transmission [43, 47]. Finally, in wideband non-Foster matching networks, circuit stability is another problem that has to be taken care of [43, 48].

The major source of loss in ESAs is the loss in the impedance matching networks. The matching network for an ESA, which is highly reactive, needs to cancel out the large

[1]Class A, class B, and class C circuits conduct 100%, 50%, and less than 50% of the input signal, respectively.

[2]Under the high Q condition, a large circulating currents is generated between the antenna and the matching circuit. Similarly, large voltage standing waves are produced within the matching circuit.

reactance and match the input impedance of the antenna to 50 Ω. If the matching network is composed of lump elements (discrete inductors/capacitors), requirements for matching such a highly reactive antenna will produce very large circulating currents and/or high standing voltages (i.e. multiple reflections) between the antenna and the matching circuits. This magnifies the intrinsic matched loss to a much larger realized loss which results in low transmission efficiency [47]. Moreover, due to the small radiation resistance (R_r) and large reactance (X_a) of the high Q ESA, only a small fraction of the applied voltage/current reaches the radiation resistance. Consequently, the matching circuit has to build up a very large voltage or current swing at the ESA terminal in exchange for even low radiated power. The stability of non-Foster transmitting systems is a another major concern due to the use of active components in these systems. It is very critical that the stability of these systems is ensured to avoid spurious radiation from the antennas. Addressing more than one of these challenges will be extremely difficult, but also a major breakthrough for electrically-small transmit applications, especially for those operating in the HF and lower VHF frequency bands (e.g. military communication systems, electronic warfare applications, etc.).

1.4 Thesis Overview

Our three approaches to investigate bandwidth enhancement and miniaturization techniques for ESAs are discussed in Chapters 2–4:

Chapter 2

A low-profile, compact spiral antenna with a broadband circularly polarized (CP) response is designed. This antenna achieves compact and miniaturized dimensions by employing a novel loading structure, where each arm of this two-armed spiral antenna is both inductively and capacitively loaded. Additional miniaturization is

achieved by using high dielectric constant superstrate and substrate materials. Using these techniques, the proposed antenna occupies a volume that is 89% smaller than that occupied by a conventional ground-plane-backed Archimedean spiral antenna with the same fractional bandwidth. Section 2.1 provides a detailed discussion about the work that was done taking this approach.

Chapter 3

We examine how a platform-mounted antenna can be used to magnetically excite the natural resonant modes of the platform and improve the bandwidth of platform-mounted antennas. In our studies discussed in Section 3.1, we show that the bandwidth of these antennas can be enhanced by increasing the excitation efficiency of the desired platform mode. This is despite the fact that the maximum linear dimensions of the structure (i.e. the feed antenna(s) and the platform) are not changed. The feasibility of using the proposed approach in designing platform-mounted HF antennas with enhanced bandwidth is experimentally verified, and is applied to a realistic armored personnel carrier. In this part of the dissertation, we demonstrate a method to exceed the bandwidth limitation of an employed ESA.

Chapter 4

Antennas for HF and VHF communication systems and electronic warfare are mostly electrically small. Due to the small radiation resistances and large reactances of ESAs, passive Foster matching for these antennas results in narrow bandwidth or low gain. Active non-Foster matching circuits produce negative reactances which allows for bypassing the gain-bandwidth limitations. However, most non-Foster

matching circuits are either unstable or do not offer the highest transmission efficiency. When functioning in a transmit application, the non-Foster matching circuits also have to meet the challenge of generating a large voltage/current swing at the ESA terminal in order to radiate even low to moderate power. In this chapter, we present a new non-Foster matching network for electrically-small monopole antennas in low-power transmit applications. The proposed antenna achieves wide bandwidth, high transducer power gain, and stability at the same time. The architecture of the proposed non-Foster matching circuit consists of a common-base amplifier, a transformer, and a negative impedance converter (NIC). In the example presented in this paper, this transmit circuit is used to match a 12.59" high monopole antenna (0.028λ at the lowest operating frequency, 26 MHz) that functions in the HF/VHF frequency band. Our experimental results show that the non-Foster transmitting system remains stable within the operating frequency band (26 MHz–89 MHz), and that the transmission efficiency (transducer power gain) of this system was successfully enhanced throughout this frequency band by up to as much as 34.4 dB using the proposed non-Foster circuit. The measured 6 dB return loss fractional bandwidth of this system is 110%, while the maximum bandwidth that can be achieved using passive matching for the same system is 0.076% at 26 MHz.

Chapter 5

This chapter discusses possible extensions of our work.

Chapter 2

A Compact, Broadband Spiral Antenna With Unidirectional Circularly Polarized Radiation Patterns

2.1 A Compact, Broadband Spiral Antenna With Unidirectional Circularly Polarized Radiation Patterns

A low-profile, compact spiral antenna with a broadband circularly polarized response is presented. The antenna is backed by a ground plane and has uni-directional radiation patterns over its entire frequency band of operation. This antenna is a multilayer structure composed of a center-fed modified Archimedean spiral that exploits a novel loading structure, a ring-shaped absorber, and a feeding network which includes a 180° power splitter. The loading structure possesses both inductive and capacitive characteristics, which increase the equivalent electrical length of the antenna while maintaining its maximum dimensions. The Archimedean spiral is integrated into the multilayer dielectric structure along with its differential feeding network. An optimized ring-shaped absorber is used on the periphery of the antenna to reduce the ground effects on the antenna performance. The proposed antenna occupies a volume that is 89% smaller than that occupied by a conventional ground-plane-backed Archimedean spiral antenna. At its lowest frequency of operation, the antenna has electrical dimensions of $0.21\lambda_{min} \times 0.21\lambda_{min} \times 0.09\lambda_{min}$, where λ_{min} is the free-space wavelength at the lowest frequency of operation (0.5 GHz). Over the frequency range from 0.5 to 1.4 GHz (2.8:1), the antenna has a VSWR of 2.4:1, and it has a circularly-polarized radiation pattern with an axial ratio better than 1.2 dB. Within this frequency range, the antenna has minimum and maximum realized gain values of -5.0 dBiC and 3.1 dBiC, respectively.

2.1.1 Introduction

Compact and broadband antennas have a wide spectrum of applications in commercial and military wireless systems. Numerous techniques for designing such antennas have been reported in the past [49]– [51]. In many applications, broadband antennas with

circularly-polarized (CP) radiation characteristics are needed. Examples include Global Navigation Satellite Systems, mobile satellite services, satellite communications, and certain radio-frequency identification applications [52]– [56]. A number of different techniques for designing broadband circularly-polarized antennas have been examined in the past [57]– [60]. Among such antennas, spiral antennas have received a significant amount of attention over the past several decades due to their ultra-wideband (UWB) characteristics and reasonably compact and low profile dimensions [51]. A two-arm Archimedean spiral antenna that has a constant input impedance and circularly-polarized radiation patterns over a wide range of frequencies was proposed by Kaiser in 1960 [51]. In this traditional antenna, the lower and upper frequencies of operation are determined by the outer and inner radii of the spiral, respectively. The frequency response of this spiral antenna also depends on the growth factor of the spirals, as well as the line widths and the truncation effects in the finite spirals. From a practical point of view, when designing a spiral antenna, the growth factor and the line width can easily be determined by referring to the design rules of the printed circuit board fabrication method used, which determine the lower bounds of the line and slot widths. Following these design rules and the guidelines for standard lithography techniques for fabricating printed circuit boards[1], the maximum linear dimension of a bi-directional Archimedean spiral antenna (that provides CP radiation with an axial ratio better than 3 dB) can be calculated as approximately $0.38\lambda_{min}$, where λ_{min} is the free-space wavelength at the lowest frequency of operation of the spiral antenna [51]. Such a conventional Archimedean spiral antenna, however, has bi-directional radiation patterns. In many applications, this is not desirable since the antenna needs to be mounted on a large metallic platform. To achieve uni-directional radiation patterns,

[1]The following are typical design rules in fabricating printed circuit boards: The minimum line width is 0.005", the minimum trace to trace spacing is 0.005", and the minimum diameter of drilled non-plated holes is 0.010".

the spiral antenna can be placed over a ground plane at a distance of $\lambda_{min}/4$ [61]. Therefore, a conventional circularly-polarized, uni-directional Archimedean spiral antenna has electrical dimensions of $0.38\lambda_{min} \times 0.38\lambda_{min} \times 0.25\lambda_{min}$ at its lowest frequency of operation. While such an antenna has a uni-directional radiation pattern, it also has a relatively high overall profile, which may not be desirable in many low-frequency (e.g. VHF and UHF) applications. Other techniques for achieving uni-directional radiation patterns in spiral antennas have also been examined [62]– [64]. Among all uni-directional antennas, ground-backed and cavity-backed antennas can be most easily mounted on metallic platforms. One of the challenges of designing ground-backed or cavity-backed antennas is to prevent strong mutual coupling between the antenna and the ground or the cavity. The coupling leads to axial ratio deterioration. A number of different researchers proposed using absorbers to decrease these mutual coupling effects [62, 65]. Other researchers utilized electromagnetic band-gap (EBG) structures or artificial magnetic conductors (AMC) in uni-directional spiral antennas [64]. Several ground-backed and cavity-backed antennas are compared in Table 2.1. These antennas either demostrate broadband responses or have compact sizes. However, having both of these criteria in a single antenna is highly desirable in many applications. To address this growing need, spiral antenna miniaturization techniques are needed.

A number of different spiral antenna miniaturization techniques have been examined in the past [24]– [20]. These techniques can be categorized into three classes: inductive loading (series inductance), capacitive loading (shunt capacitance), and slow-wave treatments (series inductance and shunt capacitance). Inductive loading increases the inductance per unit length of the spiral arms. Some of the well known realization methods are: using a series of lumped inductors along spiral arms [28], using 2-D meandering lines [24]– [26], [20], and using 3-D coils [29]. Similarly, capacitive loading increases the capacitance per unit length of the spiral arms. This can be realized by using dielectric

material loading [20] and tapered dielectric loading [27]. The slow-wave treatment is a combination of inductive and capacitive loading. It increases both the series inductance and the shunt capacitance per unit length. In [29], the slow-wave treatment was realized by using 3-D coils in combination with dielectric loading.

In this paper, we present a miniaturization technique that takes advantage of several size reduction methods simultaneously, and can be applied to Archimedean spiral antennas. Using this technique, the volume occupied by a uni-directional Archimedean spiral antenna can be reduced to $0.21\lambda_{min} \times 0.21\lambda_{min} \times 0.09\lambda_{min}$. This corresponds to a volume reduction factor of 89% compared to a conventional ground-plane-backed Archimedean spiral antenna (Conservatively, such an antenna has electrical dimensions of $0.38\lambda_{min} \times 0.38\lambda_{min} \times 0.25\lambda_{min}$ at its lowest frequency of operation). The proposed miniaturization technique is based on loading the spiral arms at their ends with a slow-wave structure possessing both capacitive and inductive elements. This increases the effective electrical lengths of the arms, thereby reducing the lowest frequency of operation of the antenna while maintaining its maximum linear dimensions. A ground plane is placed underneath the antenna to achieve uni-directional radiation. To further miniaturize the antenna and to decrease the spacing between the ground plane and the main radiator, the antenna and the ground plane are separated with dielectric substrate with a relatively high dielectric constant, ϵ_r. Since doing this results in confinements of the antenna fields in the region below the plane of spiral, the antenna is also loaded with a thick, high-ϵ_r superstrate to enhance its radiation efficiency. To mitigate the adverse effects of the ground plane's presence on the axial ratio of the antenna, a ring-shaped absorber is placed on the periphery of the antenna. The antenna is fed with differential semi-rigid coaxial cables. A prototype of the proposed antenna operating in the frequency range of 0.5-1.4 GHz is designed, fabricated, and measured. The fabricated prototype shows a minimum realized gain of -5.0 dBiC, a maximum realized gain of 3.1 dBiC, a VSWR better than 2.4:1, and

an axial ratio of 1.2 dB over this broad frequency band. In what follows, the details of the design and the principles of operation of the antenna are presented and discussed.

2.1.2 Antenna Design

2.1.2.1 Antenna Structure

Fig. 2.1 shows the cross sectional and the top views of the proposed antenna. Unlike a conventional Archimedean spiral antenna, the two arms of the proposed antenna are located on two different sides of a dielectric substrate ("sub 2" in Fig. 2.1). The inner and outer radii of the spiral antenna with loading structure are 1 mm and 60.6 mm, respectively. The spiral arm width and the gap between two adjacent arms are 1 mm. There are 13 turns of spiral arms and 1.5 turns of loading structure as shown in Fig. 2.1. Two dielectric substrates with the thickness of 25.4 mm and dielectric constants of $\epsilon_r = 10.2$ sandwich the spiral antenna ("sub 1" and "superstrate" in Fig. 2.1). Sub 1 and the superstrate are both composed of ten stacked layers of RT/duroid-6010.2LM substrates (from Rogers Corp.), each with a thickness of 2.54 mm. A ground plane is placed behind the antenna (on metal layer 1), on the bottom side of a thin dielectric substrate, to make the radiation patterns uni-directional. The feed network is composed of two semi-rigid cables as shown in Fig. 2.1. The dielectric substrate immediately on top of the ground plane has a thickness of 0.508 mm and a dielectric constant of 2.2 (RT/duroid 5880 from Rogers Corp.). The feed network is composed of two 50 Ω semi-rigid coaxial cables as shown in Fig. 2.1. The semi-rigid cables are connected to SMA connectors and are used to feed the antennas. One of the semi-rigid cables extends all the way through the thickness of substrate 1 and its center conductor is connected to the feed point of spiral arm 2 (located on metal layer 2 as shown in Fig. 2.1). The other semi-rigid cable extends all the way through the thicknesses of substrates 1 and 2, and its center conductor is connected to the feed point of

the spiral arm 1 (located on metal layer 3 as shown in Fig. 2.1). The distance between the centers of the two semi-rigid cables is 2.2 mm and the diameter of each semi-rigid cable is 2.2 mm. The outer conductors of the semi-rigid cables are connected within the region ranging from the ground plane (metal layer 1), the "sub-feed", and all the way to 1 mm below metal layer 2. The outer conductors of the semi-rigid cables are also connected to the ground plane (metal layer 1). The holes accommodating the two semi-rigid cables are extended all the way through the thickness of superstrate as well, even though the semi-rigid cables terminate on the two sides of substrate 2. This is done for two reasons. First, it provides a means for aligning different stacked dielectric substrates that constitute the superstrate. Second, the holes provide additional space for the center conductor of the semi-rigid cables to extend beyond the plane of the spirals. This extended length of the center conductors provides a reactive impedance in parallel with the feed point impedance of the spiral and can be used for impedance tuning purposes. A ring-shaped absorber is placed on the periphery of the antenna between metal layer 2 and the "sub-feed". The inner and outer diameters of the ring-shaped absorber are 80 mm and 127 mm, respectively. The height of the absorber is 25.4 mm, which is the same as substrate 1. The circular absorber is made of ECCOSORB LS-26 (from Emerson & Cuming Microwave Products, Inc.) as shown in Fig. 2.1. The overall height of the multilayer structure is 52 mm and its diameter is 127 mm.

2.1.2.2 Innovation

The design process of the antenna started with an Archimedean spiral structure, where unlike conventional spirals, each arm of the spiral is placed on one side of a relatively thin dielectric substrate. To help decrease the physical separation between the ground plane and the spiral, a dielectric substrate with a dielectric constant of $\epsilon_r = 10.2$ was used below the antenna. This also helps with reducing the electrical dimensions of the antenna. To

improve the radiation efficiency of the antenna and ensure that the fields are not confined between the antenna and the ground plane, a thick superstrate with the dielectric constant of $\epsilon_r = 10.2$ is used to load the antenna as well. To further miniaturize the antenna, a new type of a slow-wave loading structure was designed that possesses both inductive and capacitive characteristics (see Fig. 2.1) and takes advantage of the fact that each arm of the spiral is printed on a different side of the dielectric substrate. This loading structure is in the form of two meandered lines with variable (modulated) widths that overlap each other on the periphery of the spiral. Each meandered line is connected to the end of an arm of the spiral. The narrow and wide sections of the meandered lines act respectively as distributed inductive and capacitive loads of a slow-wave structure. Unlike a conventional Archimedean spiral antenna, the two arms of this spiral are fabricated on the two different sides of the dielectric substrate. This helps further increase the capacitive loading effects of the meandered section as it allows for the meandered sections of each arm of the spiral to overlap with those of the other arm in the capacitive regions (see Fig. 1). This overlapping further increases the capacitance per unit length of the capacitive sections of the meandered spiral length resulting in further increasing of the electrical length of the structure for a given physical size. This slow-wave structure increases the electrical length of the spiral for a given physical length. To compare the performance of this slow-wave structure with other common structures, we conducted full-wave EM simulations of a conventional two-wire transmission line, a zig-zag lines of the type reported in [24], and our proposed structure. Considering the two-wire line as the baseline, the zig-zag line provides a 13% reduction in the phase velocity whereas our proposed structure provides a 54% reduction. The broadside-coupled meandered loading structure can be specified mathematically using (2.1).

$$L = \alpha \times \text{square}(\beta \times \theta) \tag{2.1}$$

where square is a function for square wave generation in Matlab, α is 0.6, β is 128 and θ is measured from the z-axis. The size of arm 1 and arm 2 of the spiral antenna are determined by the (2.2) and (2.3), respectively.

$$r_1 = r_0 + b \times \theta^{(1/n)} + L \tag{2.2}$$

$$r_2 = r_0 + b \times \theta^{(1/n)} - L \tag{2.3}$$

where r_0 is 39.37 mils (1 mm), b is $78.74/\pi$ mils ($2/\pi$ mm), n is 1, and θ is measured from the z-axis.

To achieve a uni-directional radiation pattern, the antenna is backed by a ground plane. In a ground-plane backed spiral antenna, the strong coupling between the antenna and the ground plane is a common problem which can severely degrade the antenna's radiation characteristics, especially its axial ratio. In the past two decades, a variety of research groups studying cavity-backed antennas have tried to reduce the ground effects [65]– [73]. One common method used for alleviating the ground effects is to use absorbers [65]. Using absorbers decreases the mutual coupling between the ground plane and the antenna. In general, this improves the axial ratio of the antenna but it will naturally result in some gain reduction. To balance the trade-off between these two radiation characteristics, the absorber was designed as ring-shaped and is placed only on the periphery of the spiral arms. The inner diameter of the ring-shaped absorber is 80 mm and its width is 23.5mm. These dimensions are determined using trial and error simulations in CST Microwave Studio. In these simulations, an attempt was made to balance the tradeoff between the axial ratio improvement and the realized gain degradation of the antenna. To achieve the desired mode of operation, the two arms of the antenna must be fed with the same magnitude and a 180° phase difference between them. This is accomplished using the feed network shown in Fig. 2.2. In this case, the two ports of the antenna are excited using a power divider/phase

shift network. At VHF/UHF frequencies, commercially available 180° power splitters can be used to easily feed the antenna in the desired mode of operation.

2.1.3 Simulation and Measurement Results

The spiral antenna discussed in Section 2.1.2 was simulated in CST Microwave Studio. The main physical and geometrical parameters of the antenna are presented in Section 2.1.2. The antenna is simulated as a two-port device where each port is placed at the input port of one of the semi-rigid cables shown in Fig. 2.2. After each simulation, the results of the two-port full-wave EM simulations are combined to obtain the simulation results of the antenna when it is fed with a broad band 180° power splitter.

Using full-wave EM simulations in CST Microwave Studio, the electric current distribution on the spiral arms were first examined. These results confirmed that the electric currents flowing in the overlapping sections of the meandered arms are out of phase and flow in opposite directions. Therefore, the overlapped sections of the meandered spiral arms act similar to a two-wire transmission line with enhanced capacitance per unit length. Additionally, the narrow sections of the meanders have increased inductance per unit lengths. Therefore, the meandered sections of the spiral arms act as slow-wave structures with increased capacitance and inductance per unit length. The current distribution on the antenna arms is simulated and the results are shown for 0.6 GHz, 1 GHz and 1.4 GHz in Fig. 2.3. As can be observed, at each frequency, the current magnitude on the spiral arms decay as one moves from the center towards the edges of the spiral. This is an indication that standing waves on spiral arms are not significant and consequently, a low axial ratio is expected. After completion of the design process and fine tuning of the physical and geometrical parameters of the antenna, a prototype of the proposed antenna was fabricated. The spiral antenna was fabricated using chemical etching. We prepared 20 panels of 0.1” thick RT/duroid 6010.2LM substrates. Ten of which were cut into the

diameter of 127 mm (superstrate), and the rest into the diameter of 80 mm (sub2). We also prepared 4 panels of 6.35 mm thick ECCOSORB LS-26 absorbers. The absorbers were cut into ring shape with outer and inner diameters of 127 mm and 80 mm, respectively. Four additional pads were left on each layer for tightening with nylon screws and nuts.

The input reflection coefficient of the fabricated prototype was characterized using a vector network analyzer. Figs. 2.4(a) and 2.4(b) show the simulated and measured input VSWRs of the antenna as seen from the inputs of ports 1 and 2, respectively. As can be observed, a relatively good agreement between the measurement and simulation results is observed. The measured two-port S-parameters of the antenna were also post processed to calculate the input VSWR of the antenna as seen from the input of the broadband 180° power splitter shown in Fig. 2.2 and the results are presented in Fig. 2.5. As can be observed, the antenna shows a VSWR of 2.4:1 over its entire frequency band of operation.

The radiation characteristics of the antenna were measured in a multi-probe, spherical near field system over the frequency range of 0.6 GHz to 1.4 GHz. The measurements are conducted in two steps. First, the radiation characteristics of the antenna were measured when it was fed at port 1 while the second port was terminated with a matched load. Using the near-field system, the complex (magnitude and phase) far-field radiation parameters of the antenna were determined. Subsequently, a similar procedure was followed and the complex far-field radiated fields of the antenna were measured when the antenna was fed at port 2 while port 1 was terminated. These measured results were then post processed to obtain the radiation patterns of the antenna and its other radiation characteristics when the antenna is differentially fed using the feed network shown in Fig. 2.2. Since the spherical near-field measurement system used in these experiments provides us with all the complex far-field components, the process of combining the measurement results of the two-ports is straightforward. The measured electric fields from each port were summed up with 180° phase difference in Matlab. The axial ratio (the ratio of the major axis to the

minor axis) was calculated by the combined electric fields in Matlab. Fig. 2.6 shows the measured radiation patterns of the antenna over the frequency range of 0.6 to 1.4 GHz along with the simulated results. Measured and simulated results are shown for both the co-pol (RHCP) and cross-pol (LHCP) components of the radiated fields in two different cut planes ($x-z$ and $y-z$ planes). The cross-pol components are approximately 24 dB below the co-pol components in the direction of maximum radiation indicating a relatively good polarization purity. Moreover, the antenna's radiation patterns remain consistent across its entire frequency band of operation. In a real life scenario, the proposed antenna should be fed with a single feed network that provides the necessary excitation amplitude and phase over a wide frequency range. In reality, such feed networks may have amplitude and/or phase imbalances at some frequencies over the band of operation. This will result in the deterioration of the axial ratio of the antenna and its polarization purity compared to what is reported in this paper.

Fig. 2.7 shows the measured and simulated axial ratios of the antenna along the direction of maximum radiation. As can be observed, the antenna demonstrates an axial ratio of lower than 1.2 dB across its entire band of operation. The simulated and measured realized gains of the antenna are shown in Fig. 2.8. The simulated and measured maximum realized gains of the antenna are 3.3 dBiC and 3.1 dBiC, respectively. Assuming that the minimum acceptable realized gain is -5.0 dBiC, the maximum acceptable axial ratio is 3.0 dB, and the maximum acceptable VSWR is 2.5:1, the bandwidth of the antenna is determined to be from 0.5 GHz to 1.4 GHz (a 2.8:1 bandwidth). At the lowest frequency of operation of 0.5 GHz, the antenna has maximum electrical dimensions of $0.21\lambda_{min} \times 0.21\lambda_{min} \times 0.09\lambda_{min}$. A conventional spiral antenna with a performance similar to the proposed antenna is also designed as a reference. It has electrical dimensions of $0.38\lambda_{min} \times 0.38\lambda_{min}$ (diameter=228.6 mm). To make this antenna uni-directional, a

ground plane is placed a quarter wavelength below the antenna [61]. The simulation results of this antenna are shown in Figs. 2.5, 2.7, and 2.8. The electrical volume occupied by this antenna is thus, $0.38\lambda_{min} \times 0.38\lambda_{min} \times 0.25\lambda_{min}$. Notice that placing a ground plane below an Archimedean spiral antenna deteriorates its performance (i.e. axial ratio and gain) and generally shifts the lowest operation frequency of the antenna up. However, to be conservative in our comparison, we have considered the electrical volume of $0.38\lambda_{min} \times 0.38\lambda_{min} \times 0.25\lambda_{min}$ as the reference for calculating the volume reduction factor of our proposed antenna, 89%.

2.1.4 Conclusion

In this paper, a low-profile ground-backed spiral antenna with a wideband circularly-polarized response was presented. The proposed spiral antenna achieves compact and miniaturized dimensions by employing a novel loading structure where each arm of the antenna is both inductively and capacitively loaded. Additional miniaturization is achieved by using high dielectric constant superstrate and substrate materials. Using these techniques, the antenna diameter is effectively reduced to $0.21\lambda_{min}$. In order to reduce the effects of the ground plane placed in close proximity of the antenna, an optimized ring-shaped absorber is placed between the antenna and the ground plane. The bandwidth of this antenna is from 0.5 GHz to 1.4 GHz, over which the antenna shows an axial ratio of 1.2 dB, a VSWR of 2.4:1, and minimum and peak realized gain values of -5 dBiC and 3.1 dBiC, respectively. One of the advantages of the proposed multi-layer structure presented in this paper is the potential integration of miniaturized-element frequency selective surfaces of the types reported in [74]– [75] within the superstrate layers of the antenna. This possibility is currently being explored for developing modified versions of the proposed antenna that demonstrate significantly reduced out of band radar cross sections and can be used for low-observable applications.

Table 2.1 Comparison of the proposed antenna with a number of different cavity-backed and ground-backed antennas reported in the literature. Bandwidth is determined based on the frequency range where the axial ratio is less than 3 dB and the realized gain is higher than -5 dBiC.

Ref.	H	L	W	BW	Peak Gain
[66]	0.18	0.86	0.86	15%*	8.7 dBiC
[67]	0.07	0.38	0.38	79%**	3 dBiC
[68]	0.09	0.22	0.22	13%	2.9 dBiC
[69]	0.22	1.14	0.66	22%*	9 dBiC
[70]	0.07	0.80	0.80	100%	8.5 dBiC
[71]	0.27	1.52	1.52	50%	11.0 dBiC
[72]	0.30	0.85	0.85	4%*	7.1 dBiC***
[73]	0.25	1.03	1.03	55%	9.9 dBiC
Here	0.09	0.21	0.21	95%	3.4 dBiC

* Only 3 dB axial ratio is reported and used to determine the bandwidth.

** Only realized gain is reported in the paper and is used to determine the bandwidth.

*** 7.1 dBiC (LHCP), 4.9 dBiC (RHCP).

**** The unit of H, L, and W is λ_{min}.

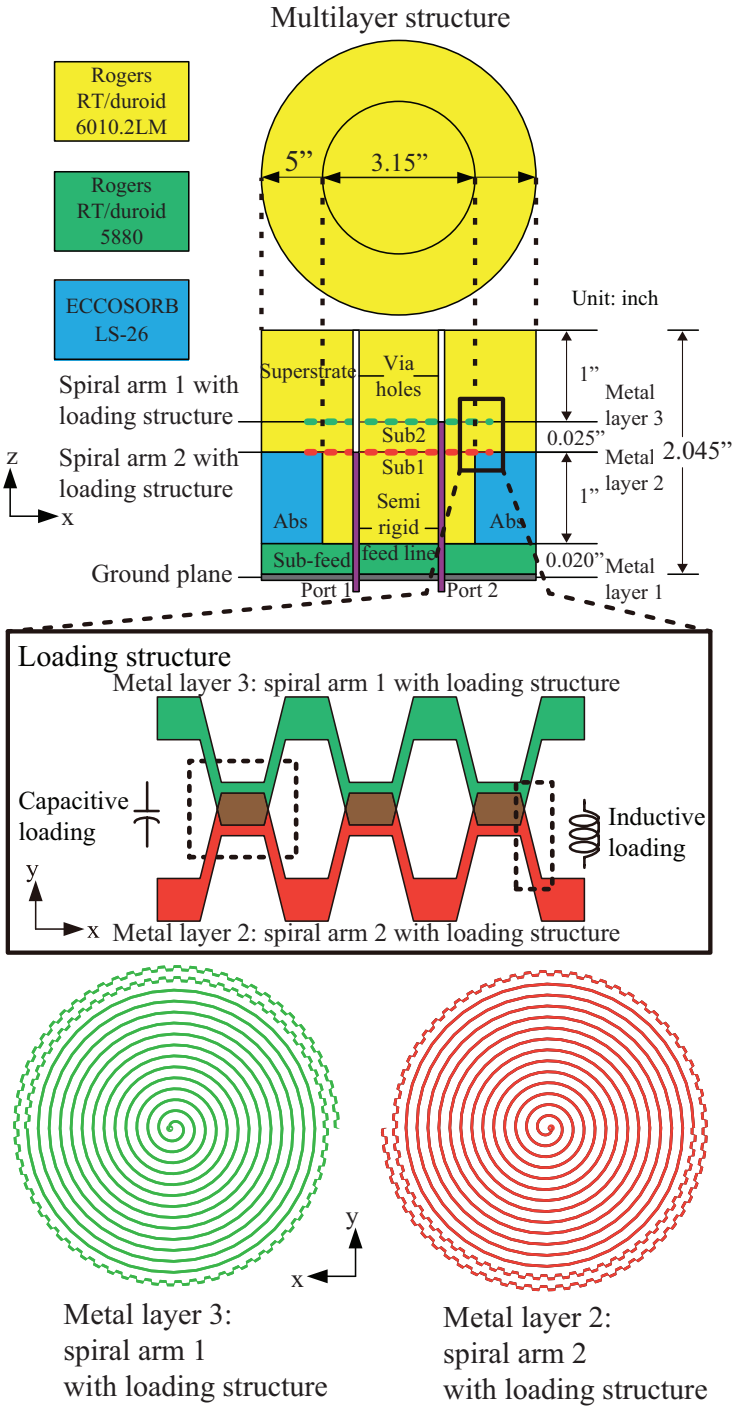

Figure 2.1 Topology of the proposed ground plane backed ultra-wideband spiral antenna.

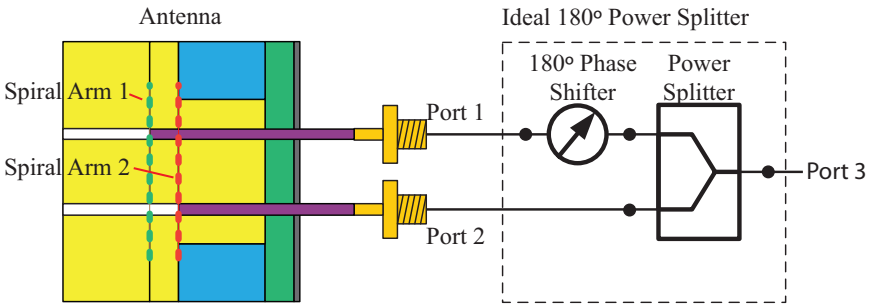

Figure 2.2 The proposed UWB spiral antenna is fed with an ideal 180° power splitter which provides differential feeding at the two ports.

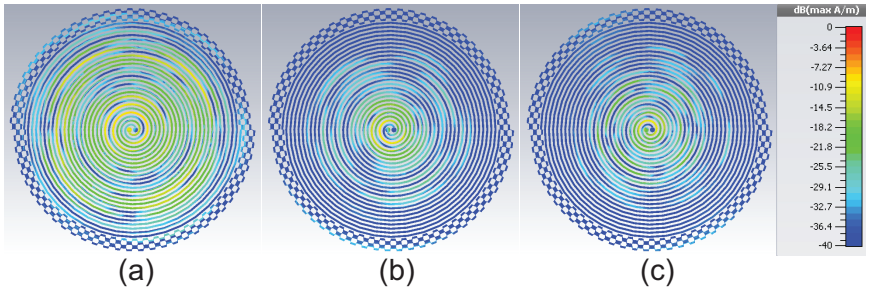

Figure 2.3 Simulated surface current distributions of the antenna at (a) 0.6 GHz, (b) 1.0 GHz and (c) 1.4 GHz.

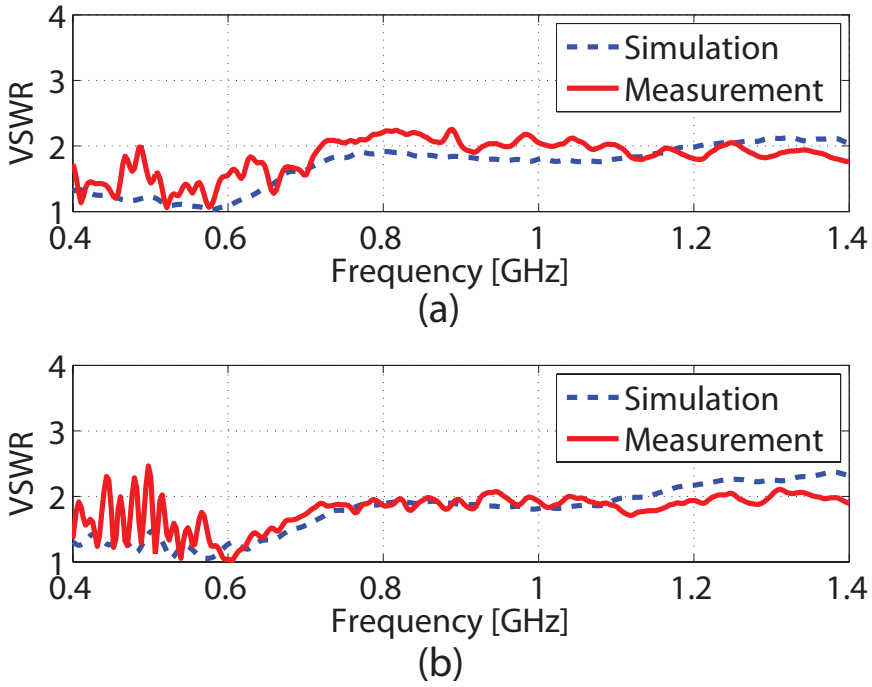

Figure 2.4 Simulated and measured VSWR of the antenna (a) at port 1 when port 2 is terminated with a 50 Ω load; and (b) at port 2 when port 1 is terminated with 50 Ω load..

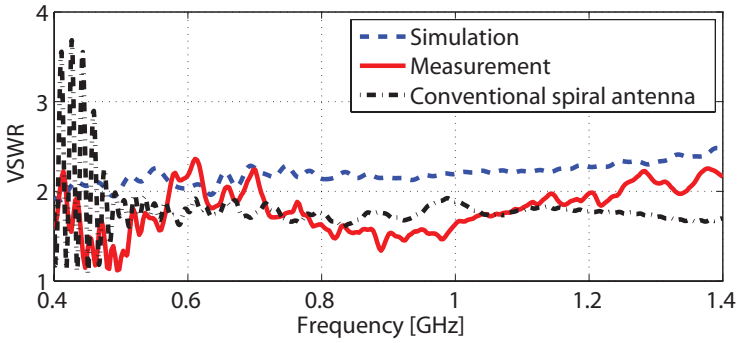

Figure 2.5 Simulated and measured VSWR of the antenna as seen from the input port of the feed network shown in Fig. 2.2.

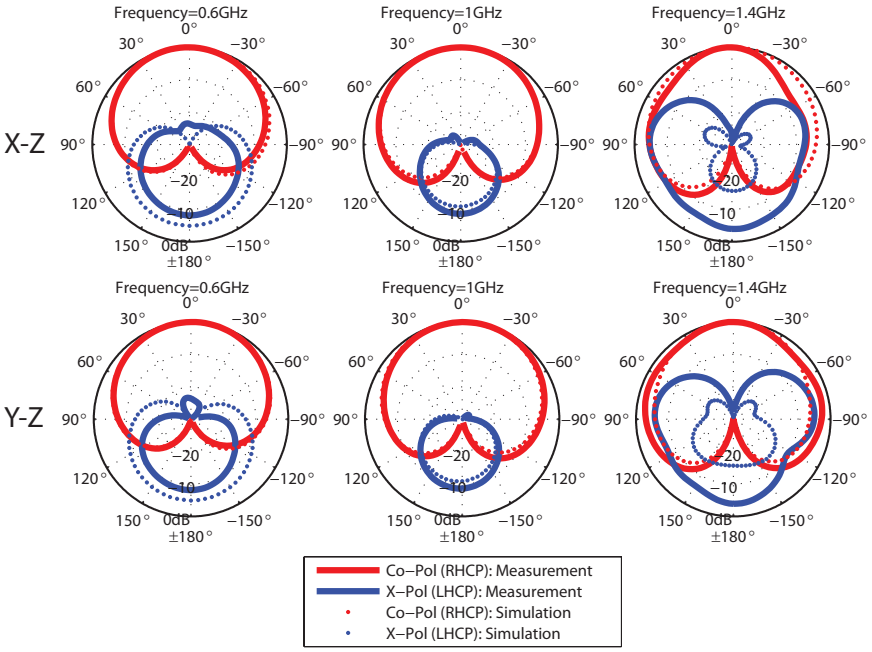

Figure 2.6 Simulated and measured radiation patterns of the antenna in the $x-z$ and $y-z$ planes.

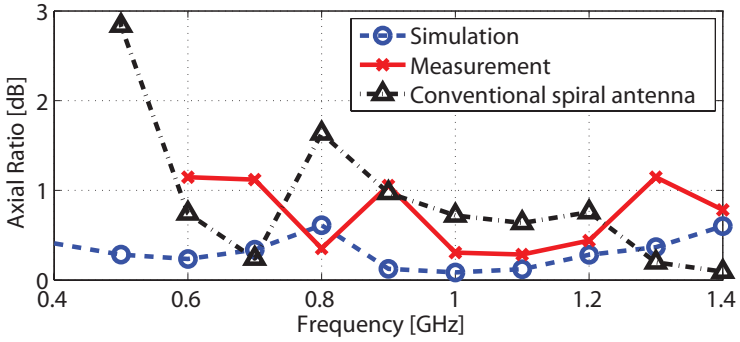

Figure 2.7 Simulated and measured axial ratios of the antenna when the antenna is fed with the feed network shown in Fig. 2.2.

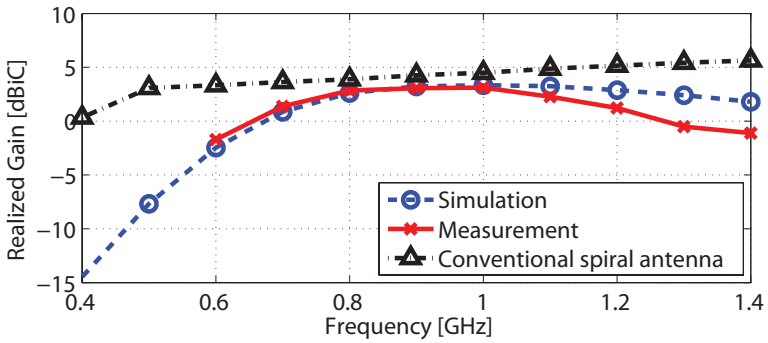

Figure 2.8 Simulated and measured realized gains of the antenna when it is fed with the feed network shown in Fig. 2.2.

Chapter 3

Bandwidth enhancement of platform-mounted HF/VHF antennas using the characteristic mode theory

3.1 Bandwidth enhancement of platform-mounted HF antennas using the characteristic mode theory

Many high frequency (HF) antennas have significantly smaller dimensions than the wavelength at which they operate and thus suffer from narrow bandwidths. In many military applications, such HF antennas are mounted on relatively large metallic platforms. In this paper, we examine how a platform-mounted antenna can be used to excite the characteristic modes of the platform itself to increase the overall bandwidth of the system. In this case, the platform will act as the main radiator and the mounted antennas act primarily as the coupling mechanism between the antenna and the external circuit. We use the theory of characteristic modes to identify the appropriate platform modes and determine the practical means of exciting them. This allows for significantly increasing the bandwidth of the antenna system compared to the bandwidth of the antenna system in isolation. This approach is employed to enhance the bandwidth of a horizontally-polarized HF loop antenna system by as much as 10 times compared to a stand-alone full loop antenna. Scaled models of the proposed antennas were fabricated and experimentally characterized. Measurement results are in good agreement with the theoretically predicted results and demonstrate the feasibility of using the proposed approach in designing bandwidth-enhanced platform-mounted HF antennas.

3.1.1 Introduction

The high-frequency (HF) band (3-30 MHz) is used for various military applications including communications and electronic warfare applications [76]– [33]. In the HF band, the wavelength ranges from 100 m at the lower end to 10 m at the upper end of the band. Due to such large wavelengths, most HF antennas used for military applications tend to be electrically-small antennas (often monopole whip antennas) used in conjunction with

automatic impedance tuners. However, such electrically-small antennas tend to have very small bandwidths [1]– [2], which is a limiting factor for certain applications [78]– [79].

Since most HF antennas used for military applications are often mounted on physically large metallic platforms (e.g. ships, military vehicles, and airplanes), the presence of the platform in the vicinity of the antenna may be exploited to address the challenge of narrow bandwidth. In these situations, the platform is generally larger than the antenna mounted on it. Therefore, if the platform can be used as part of the antenna, the maximum linear dimension of the antenna can be increased significantly, resulting in an enhanced bandwidth. To do this, the platform and the antenna must be designed together and the platform must be considered to be a major part of the radiating structure from the beginning. In the past, this technique has been applied to design mobile handset antennas by exciting radiating currents on mobile terminal chassis [80]– [83]. The design of military platform-mounted antennas has also been studied, and a number of techniques for exploiting the platform to obtain enhanced performance have been reported [31], [35]– [86]. These platform-mounted antennas can be categorized into two classes: 1) Those that partially excite the platform modes [31], [35]– [38], and 2) Those that fully excite the platform modes [39]– [86]. In [31], HF fan/whip antennas are placed on the superstructure of a ship to excite currents on a portion of the ship's structure. In [35]– [36], part of the platform was used as the radiator, and part of a folded monopole antenna was replaced by the mast of a ship. In [37], half loop antennas were flush-mounted at the modified ship corners to take advantage of part of the platform as reflecting plane. In a more recent study, a characteristic-mode-based approach was employed to find desirable radiating currents from the characteristic modes of the platform [38]. To excite the desired currents on the structure, slits were cut in the body of the ship where the currents are the strongest. In [39], the theory of characteristic modes was used to determine the optimized positions of the feed probes to excite the radiating currents on an unmanned aerial vehicle.

In this paper, we present a systematic method for designing an HF antenna system that takes advantage of the presence of the platform to achieve significantly enhanced bandwidth compared to a stand-alone antenna. To conduct this study, we consider a simple metallic platform in the shape of a rectangular box with dimensions that are comparable to those of a typical military armored personnel carrier. Using the theory of characteristic modes, we examine the resonant behavior of this structure and identify the modes that can generate the desired radiation characteristics. Subsequently, we use strategically-located coupling loops, which are relatively small compared to other designs [81]– [82], [38]–[39], to excite the desired platform mode using magnetic field coupling. In this arrangement, the antenna acts as a transformer between the feed and the platform. Using magnetic field coupling between the loop and the platform allows for maintaining the platform shape intact and eliminates the need to cut holes or slits within the body of the structure. We also demonstrate that, by increasing the number of coupling loops strategically located at different locations on the periphery of the platform, a better approximation of the current distribution associated with the desired resonant mode of the platform can be obtained. This results in increasing the bandwidth of the antenna system. Specifically, we demonstrate that the proposed process can be used to improve the bandwidth of a platform-mounted antenna system that acts as a single radiator, compared to what can be achieved with the same antenna or system in isolation without the presence of the platform. By using different numbers of coupling loops, the bandwidth of the proposed platform-mounted antenna system is increased by as much as 10 times, compared to an isolated loop antenna in free space. Experiments were conducted by fabricating and characterizing scaled models of the structure. Experimental results of the scaled-model prototype closely follow the theoretical predictions. Finally, the proposed method was applied to a more realistic military platform and, using full-wave EM simulations, it was demonstrated that the conclusions obtained by using the simplified platform can also be extended to the more realistic one.

3.1.2 Antenna Design

We start by considering a simple metallic platform in the shape of a rectangular box with dimensions of 3.7 m $\times$ 10.7 m $\times$ 3.3 m. These dimensions are selected because they are comparable to the physical dimensions of a typical armored personnel carrier (Expeditionary Fighting Vehicle or EFV [87]).

3.1.2.1 Examining the Characteristic Modes of the Platform

The theory of characteristic modes was introduced and refined in the 1960s and 1970s [88]– [91]. Characteristic modes of an object are a complete orthogonal set of currents. Any induced current on the object can be expanded in terms of these modes. The radiated fields associated with these currents in the far field are also orthogonal. The eigencurrents J_n can be determined from the following generalized eigenvalue equation:

$$XJ_n = \lambda_n RJ_n \tag{3.1}$$

where *R* and *X* are the real and imaginary parts of the impedance matrix of the electric field integral equation. λ_n is the eigenvalue associated with the eigencurrent J_n. With the assumption that each characteristic mode is 100% excited by an ideal external source, the potential contribution of each mode is measured by its modal significance:

$$MS = \left| \frac{1}{1 + j\lambda_n} \right| \tag{3.2}$$

The design process of the proposed antennas starts by examining the resonant behavior of the platform and their associated current distributions. The commercial full-wave software FEKO was used to carry out the analysis of characteristic modes, and the modal significance curves of the structure examined are shown in Fig. 3.1[1]. A mode is considered

[1]FEKO numbers the characteristic modes according to their modal significance values and from low frequency to high frequency.

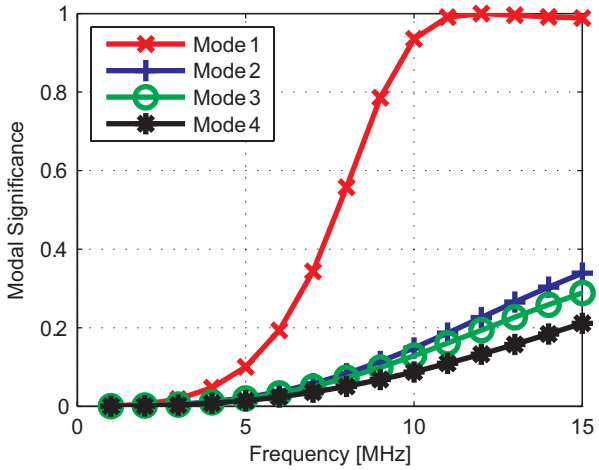

Figure 3.1 Simulated modal significances of the first four modes of the platform.

resonant when the modal significance of that mode attains a value of 1 [92], and a mode is considered significant when the modal significance is greater than or equal to 0.707 [38]. Fig. 3.1 shows that the dominant mode for this structure is mode 1, and this mode is significant above approximately 9 MHz. Fig. 3.2 shows the electric current distributions and the radiation patterns of the first four characteristic modes of the platform. Examination of the electric current distribution and radiation pattern of mode 1 indicates that it has a direction of maximum radiation towards zenith. Modes with current distributions and radiation patterns similar to those shown in Figs. 3.2(a)-3.2(b) (modes 1 and 2) are suitable for NVIS (Near Vertical Incidence Skywave) applications at HF band. In this work, we focus on exciting mode 1 because it is the dominant mode of the platform. However, the concepts presented in the subsequent sections are equally applicable to the excitation of other modes shown in Fig. 3.2.

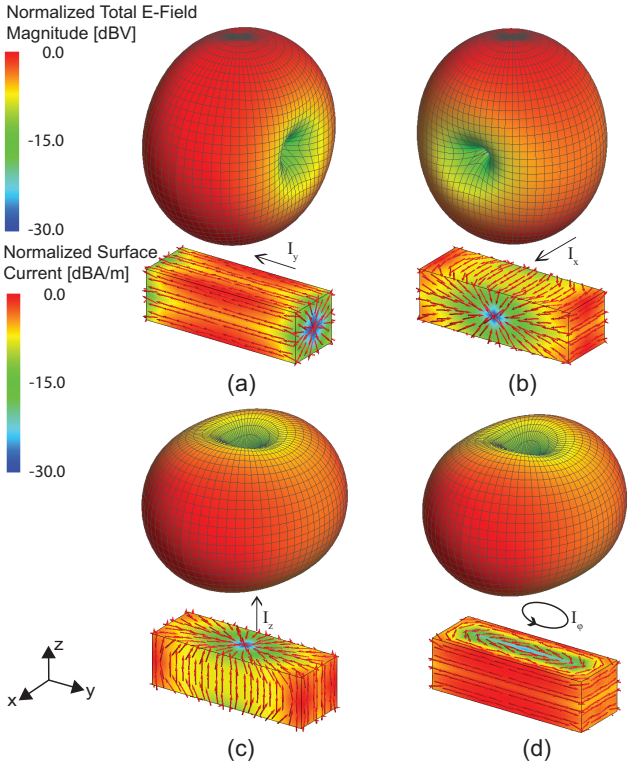

Figure 3.2 Simulated normalized current distribution and normalized radiation patterns of the first four characteristic modes of the platform. (a) Mode 1, (b) mode 2, (c) mode 3, and (d) mode 4.

3.1.2.2 Radiation Q of the Platform Modes

To examine the upper limit of the bandwidth that can be achieved by exciting the platform's characteristic modes, we need to calculate the lower bound for the Q of the desired platform mode. Given the platform dimensions and considering a frequency of operation of 10 MHz, the platform Q based on the Chu-McLean limit is calculated to be $Q_{Chu} = 1.3391$ [2], [7]. The 10 dB return loss fractional bandwidth associated with this Q is approximately 50% [7]– [19]. This, however, is too optimistic a value because the platform shape does not utilize the available volume within the Chu's sphere efficiently. Furthermore, the desired platform mode does not have the optimum current distribution needed to generate the lowest possible Q. Therefore, a more realistic calculation of the Q can be performed by examining the actual stored energy and radiated power associated with the current distribution of the desired platform mode. The radiation Q can be specified mathematically as:

$$Q = \omega \frac{2\,\text{Max}(W_e, W_m)}{P_{rad}} = 4\pi \frac{\text{Max}(W_e, W_m)}{W_{rad}} \tag{3.3}$$

where W_e and W_m are the total stored electric energy and magnetic energy, respectively, P_{rad} is the radiated power, and W_{rad} is the radiated energy. The commercial software FEKO does not automatically calculate the Q of the characteristic modes. Therefore, this was done manually by exporting the electric and magnetic fields associated with the desired platform mode. The total stored energy was then calculated numerically by evaluating the following expression [93]:

$$W_e = \frac{1}{2}[W_e^{tot} + W_m^{tot} - W_{rad}] - \frac{1}{4\omega}\text{Im}\{\sum\sum \vec{S} \cdot \vec{n}\Delta s\} \tag{3.4}$$

$$W_m = \frac{1}{2}[W_e^{tot} + W_m^{tot} - W_{rad}] + \frac{1}{4\omega}\text{Im}\{\sum\sum \vec{S} \cdot \vec{n}\Delta s\} \tag{3.5}$$

where W_e^{tot} and W_m^{tot} are the average total electric and magnetic energies, respectively, W_{rad} is the radiated energy, and $\vec{S} = 1/2\vec{E} \times \vec{H}^*$ is the complex Poynting vector.

To calculate these values, the electric and magnetic field values calculated by FEKO are exported along a rectangular grid, the cross section of which is shown in Fig. 3.3. Here, Δx, Δy, and Δz are the spatial steps along the $\hat{x}$, $\hat{y}$, and $\hat{z}$ directions along which the field values are sampled. The values of the six field components (E_x, E_y, E_z, H_x, H_y, and H_z) are computed by FEKO at each point outside of the platform on a rectangular grid as shown in Fig. 3.3. Using this, W_e^{tot} and W_m^{tot} are calculated using the following equations:

$$W_e^{tot} = \frac{\epsilon}{4} \sum_x \sum_y \sum_z (|E_x|^2 + |E_y|^2 + |E_z|^2) \Delta x \Delta y \Delta z \tag{3.6}$$

$$W_m^{tot} = \frac{\mu}{4} \sum_x \sum_y \sum_z (|H_x|^2 + |H_y|^2 + |H_z|^2) \Delta x \Delta y \Delta z \tag{3.7}$$

The expression calculated from (3.6) and (3.7), however includes the total energy (i.e., the combination of the stored energy and the radiated energy). To obtain the total stored energy, the contribution of the radiated energy must be subtracted from the total stored energy. The radiated energy is obtained using:

$$\begin{aligned} W^{rad} \;=\; & \frac{1}{c}\mathrm{Re}\{2\Delta x \sum\sum \vec{S_x} \cdot \hat{x} \Delta y \Delta z \\ & +2\Delta y \sum\sum \vec{S_y} \cdot \hat{y} \Delta x \Delta z \\ & +2\Delta z \sum\sum \vec{S_z} \cdot \hat{z} \Delta x \Delta y\} \end{aligned} \tag{3.8}$$

where $\vec{S} = 1/2\vec{E} \times \vec{H}^*$ is the complex Poynting vector and c is the speed of light. The numerical calculations expressed by (3.6)–(3.8) must be carried out over a sufficiently large volume in the vicinity of the antenna to ensure that all of the stored energy in the vicinity of the antenna is taken into account. To determine the size of the domain over which these calculations must be performed, one can increase the volume successively and monitor for the convergence of the results obtained. The mesh scheme for the Q calculations is shown in Fig. 3.3. The mesh size and the size of the computational domain

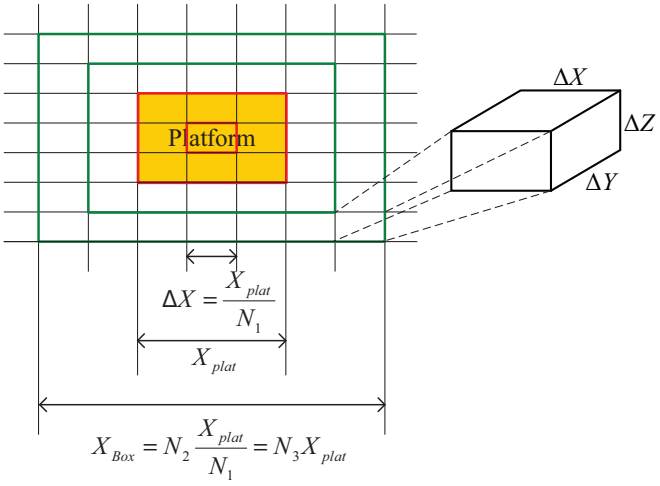

Figure 3.3 The scheme of the radiation Q calculation.

are determined by N_1 and N_3, respectively. N_2 is the number of grids along each direction ($\hat{x}$, $\hat{y}$ and $\hat{z}$). In our calculations, it was found out that $N_1 = 9$, $N_2 = 171$ and $N_3 = 19$ resulted in a computational domain large enough to allow for accurate calculation of the Q, and hence, these values were chosen to perform the Q calculations for the platform. Following this procedure, the Q of mode 1 is calculated to be $Q_{Mode1} = 8.6655$. This corresponds to a matched 10 dB return loss fractional bandwidth of 7.69% at 10 MHz. These results are summarized in Table 3.1.

3.1.2.3 Feed Structure Design

Examination of the current distribution of mode 1 of the platform reveals that the entire antenna acts as a fat dipole for this mode, as shown in Fig. 3.2(a). Such a dipole antenna can be fed by a voltage gap placed at the center of the dipole, as shown in Fig. 3.4(a). However, this requires dividing the platform in two, which is not practical. Alternatively, capacitive or inductive coupling techniques can be used to excite this mode, as shown in Figs. 3.4(b) and 3.4(c). Fig. 3.4(b) shows an example of using capacitive

Table 3.1 Comparison of simulation results of the different antennas.

Scenario[a]	f_0 (MHz)	BW	η_{tot}
Chu limit	10.00	49.79%	
Mode 1	10.00	7.69%	
One full loop alone	11.99	0.33%	97.1%
One half loop (Center)	12.32	0.64%	99.1%
One half loop (Edge)	11.48	1.31%	99.5%
Two half loops (Edge)	10.76	2.20%	99.7%
Four half loops (Edge)	10.16	3.27%	99.7%

[a] The 1 full loop antenna is stand-alone. Everything else is on the platform.

coupling elements (CCEs) to excite mode 1. In this case, two monopole antennas, fed with the same magnitudes and 180° phase difference, are used to excite mode 1. In Fig. 3.4(c), multiple half loops, all fed with the same magnitudes and phases, are placed on the periphery of the platform. The loops act as inductive coupling elements (ICEs) and couple with the magnetic field of mode 1 to excite this mode. Both of these coupling methods can be used to efficiently excite mode 1 without cutting the platform. In this work, however, we employ the ICE excitation shown in Fig. 3.4(c) for two reasons. First, we assume that the maximum linear dimension of the antenna/platform is to be maintained (i.e., the coupling antennas should not increase the radius of the Chu sphere, a, circumscribing the entire structure, as seen in Fig. 3.4(d)). With this constraint, Fig. 3.4(d) shows that within the Chu's sphere, very limited space is available to place the CCEs whereas ample space is available to accommodate the ICEs. Additionally, in a real life application, the two smaller surfaces where CCEs are located on correspond to the front and back side of an amphibious assault vehicle. Mounting long monopole antennas on these surfaces makes the antennas extremely susceptible to damage and interferes with the primary tasks that these vehicles have to perform. The presence of the loops or monopoles on the platform cause new modes to be created. However, these modes are associated with the resonances of the coupling elements themselves and become significant at higher frequencies only. Specifically, characteristic mode simulations in FEKO show that the presence of the coupling elements does not significantly impact the properties of mode 1 and its current distribution. Therefore, in the analysis conducted in the remainder of this paper, we focus on examining the characteristic modes of the platform alone.

Fig. 3.5(a) shows an example of using ICEs to excite mode 1. Here, only a single loop antenna is used to excite the desired platform mode. To magnetically excite mode 1, where the current direction on the platform is in the $\hat{y}$ direction and the H-plane of the fat dipole is on the $x-z$ plane, the ideal direction of the matched half loop antenna is on the $y-z$

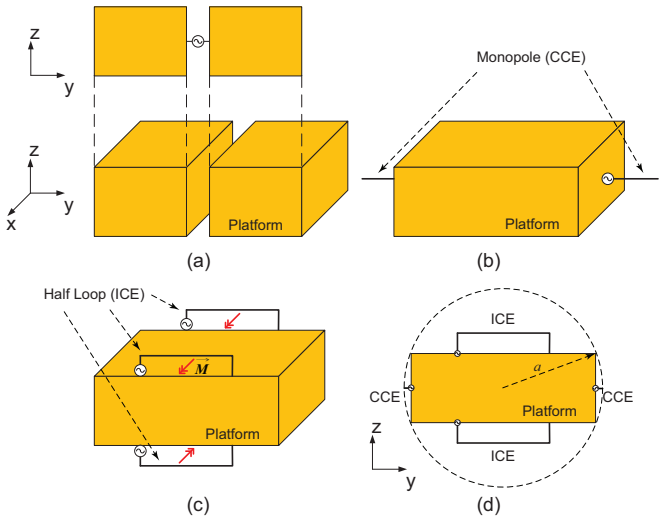

Figure 3.4 Mode 1 of the platform is excited by (a) a voltage source, (b) monopole antennas, or (c) half loop antennas. (d) Comparison of the two coupling methods with a given maximum linear dimension of the system, $2a$.

plane, as shown in Fig. 3.5(a). Fig. 3.6 shows a comparison between the input reflection coefficients of a full loop antenna in free space and the half loop antenna, shown in Fig. 3.5(a), on the platform. The simulations in both cases are conducted in FEKO. Since both loops are small, their input impedances are reactive. Each antenna is impedance matched at the frequency where the real part of its impedance is close to 50 Ω. Therefore, impedance matching can be performed using a simple, series capacitor at the input of the antenna. This simplifies the design of the antenna but also means that the frequency where the best impedance match is obtained can slightly change from one design to the other. As can be observed, while both antennas are narrow-band antennas, the platform mounted antenna exhibits a fractional bandwidth almost twice that of the free-space loop antenna (0.64% compared to 0.33%). This is due to the fact that the half loop antenna excites currents on the platform and thus has an effectively larger electrical dimension. The current distribution and the radiation pattern of the antenna shown in Fig. 3.5(a) are

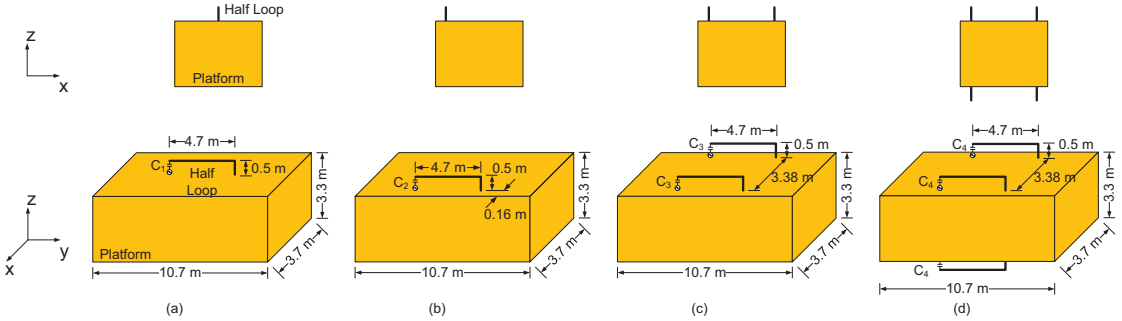

Figure 3.5 (a) One half loop antenna on the top of the platform (Center). (b) One half loop antenna on the top of the platform (Edge). (c) Two half loop antennas on the top of the platform (Edge). (d) Four half loop antennas on the top and bottom of the platform (Edge). $C_1 = 12\ pF$, $C_2 = 18\ pF$, $C_3 = 25\ pF$ and $C_4 = 32\ pF$. The wire diameter of the loops are 81.92 mm.

also calculated using full-wave EM simulations in FEKO and the results are shown in Fig. 3.7(a). As can be observed, the current distribution in this case is different from that shown in Fig. 3.2(a). This is to be expected since a single loop does not effectively synthesize the required magnetic current distribution on the periphery of the platform.

Examining Fig. 3.2(a) also reveals that the electric current density of mode 1 is the strongest at the edges of the structure. Therefore, the coupling efficiency between the single loop and the platform can be enhanced if the loop is located at the edge of the platform, as shown in Fig. 3.5(b). The simulated input reflection coefficient of this antenna is also presented in Fig. 3.6. Observe that the fractional bandwidth of the antenna is now increased to 1.31% compared to 0.64% for the single antenna mounted on the center of the platform's top surface. To further increase the efficiency of excitation of mode 1, the number of loops placed on the platform can be increased as shown in Figs. 3.5(c) and 3.5(d). This will, in turn, increase the bandwidth of the antenna system because the available volume (i.e., the platform surface) is more efficiently utilized. Fig. 3.5(c) shows a scenario where two half loops are placed on top of the platform and at its edges where the current density of mode 1 is the strongest. Fig. 3.5(d) shows a similar scenario where the number of antennas is increased to four to provide a more uniform excitation of mode 1. In both cases, all half loops mounted on the platform are excited in phase and with the same magnitudes. Fig. 3.6 shows the simulated input reflection coefficients of these antennas. Since the antenna systems were matched using a single reactive element used for each of the loops, the frequency where the internal resistance is $50\ \Omega$ varies with the different feed scenarios. Nevertheless, the frequency shift is less than 2.16 MHz, and the operating frequencies of all scenarios are still in the lower HF band. If identical operating frequencies are required, a two-element matching network can be used to eliminate the shift. Notwithstanding this, the validity of the proposed concept can still be demonstrated using the simple matching network used in this design.

The dimensions and positions of the loops, as well as the values of the commercially-available matching capacitors, are shown in Fig. 3.5 and its caption, respectively. S-parameter files of ideal two-way and four-way power splitters were used in the simulation of the antennas shown in Figs. 3.5(c) and 3.5(d), respectively, to obtain the input reflection coefficient as seen from the terminals of a single feed. As can be seen, by using multiple loops strategically placed at different locations on the platform, the bandwidth of the antenna system is considerably increased. Specifically, for the case of two loops the fractional bandwidth is increased to 2.20% and for the case of four loops, the fractional bandwidth is further increased to 3.27%. These enhancements correspond to factors of 3 (7) and 5 (10) respectively compared to the bandwidth of a single half loop (full loop) mounted on the platform (in free space). The total efficiency (η_{tot}) of the platform-mounted antennas shown in Fig. 3.5 are greater than 99% (Table 3.1), which is expected because the only source of loss considered in the simulations is the ohmic losses in the conductors. This was done deliberately because the feed network loss increases with the number of coupling loops, primarily due to the loss of the power splitters. Therefore, considering a more realistic loss scenario in the simulations makes it difficult to distinguish the main source of enhancement of the bandwidth. However, as can be observed from the ideal simulations performed here, the bandwidth of the antenna increases significantly as the number of coupling loops is increased. This confirms that the increase in bandwidth is not due to the losses of the system because all systems considered in these simulations have efficiencies close to 100%.

To demonstrate that the bandwidth enhancement is achieved by exciting the electric currents of the platform, as opposed to increasing the volume over which the four loops are placed, we examined the performance of a four-element antenna array composed of four full loops in free space, as shown in Fig. 3.8. Each loop has dimensions of 4.7 m $\times$ 1 m and the relative positions of the loops in Figs. 3.8(b)-3.8(c) are the same as those shown

in Figs. 3.5(d) and 3.8(a) in the absence of the platform. In Fig. 3.8(b), all four elements of this array are fed and impedance matched similar to what was described earlier and the same ideal 4-1 power splitter was used to feed them. Using this approach, the 10 dB return loss fractional bandwidth of this array is simulated to be 0.22%, as shown in Fig. 3.6, which is even less than that of the one full loop in free space. This is because the direction of the feed ports of the bottom two loops is 180° different from the upper two loops as is the case in the structure shown in Fig. 3.5(d). When the feed directions are the same (Fig. 3.8(c)), the fractional bandwidth becomes 0.87%, as shown in Fig. 3.6. Either way, the fractional bandwidth of the four full loops in free space is significantly smaller than the 3.27% bandwidth obtained from the structure shown in Fig. 3.5(d). This verifies that the presence of the platform and efficient excitation of the platform modes are indeed critical in achieving the enhanced bandwidths reported in Fig. 3.6. Additionally, the comparison of the bandwidths of the structures shown in Figs. 3.5(a) and 3.5(b) reveals that efficient coupling between the coupling loops and the platform is also important in enhancing the bandwidth of the antenna system. Figs. 3.7(b)-3.7(c) show the current distribution and the radiation pattern of the antennas for the cases where two and four coupling loops are used to excite the desired platform mode. Observe that by increasing the number of coupling loops, the radiation pattern and the current distribution of the structure become closer to that shown in Fig. 3.2(a). This distribution of the radiating current over a larger volume is in part responsible for the bandwidth improvement observed.

3.1.3 Experimental Results

Due to the large size of these HF antennas, conducting measurements of the full-scale versions of the proposed platform-mounted antennas is not practical in our experimental facilities. Therefore, to validate the proposed concept, scaled versions of the proposed structures were fabricated. The platforms were fabricated by 3D printing and the 3D

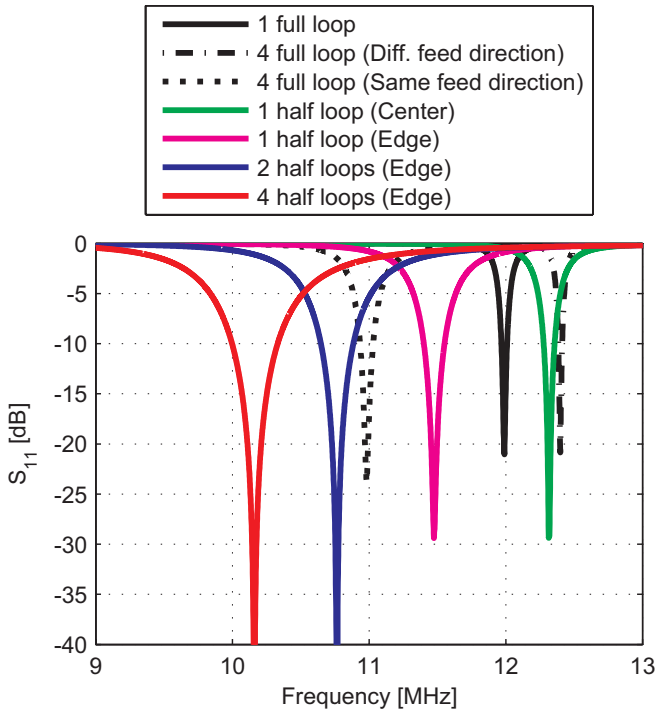

Figure 3.6 Simulated S_{11} of the platform-mounted antennas and full loops shown in Figs. 3.5 and 3.8.

Table 3.2 Comparison of measurement results of the different scaled antennas.

Scenario	f_0 (MHz)	BW	Max. D (dBi)	η_{tot}
One half loop (Center)	707.55	0.91%	4.2	26%
Two half loops (Edge)	650.00	1.78%	3.5	37%
Three half loops (Edge & Center)	634.15	1.97%	3.8	33%
Four half loops (Edge & Center)	639.60	2.84%	2.8	30%
Four half loops (Center)	672.65	3.75%	3.1	26%
Four half loops (Edge)	652.60	5.12%	3.9	32%

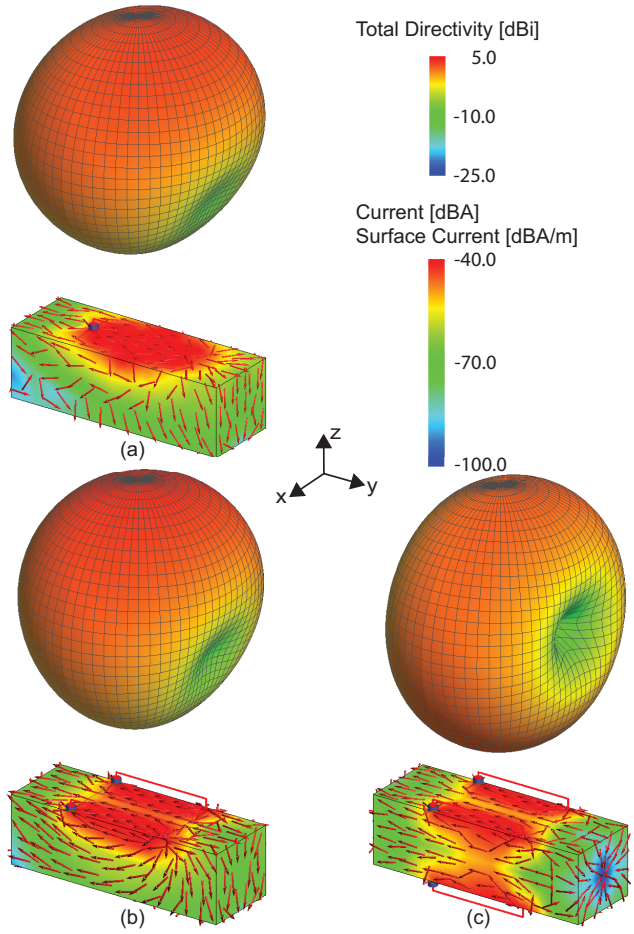

Figure 3.7 Simulated normalized current distributions and radiation patterns of the platform-mounted antennas. (a) One half loop antenna, placed on the top surface of the platform, is used to excite currents on the surface of the platform. (b) Two half loop antennas, placed at the edges of the top surface, are used to excite electric currents on the platform. (c) Four half loop antennas, two placed at the edges of the top surface and the other two placed at the edges of the bottom surface, are used to excite electric currents on the platform.

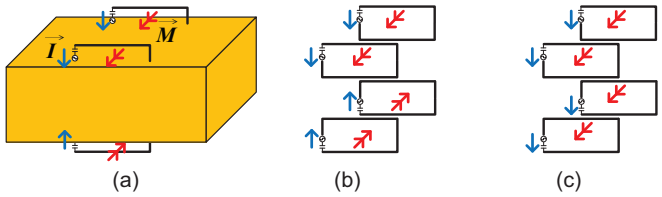

Figure 3.8 (a) Four half loops on the platform; (b) Four full loops in free space. The feed directions of the bottom two loops are 180° different from the top two loops (as in (a)); (c) Four full loops in free space (feed directions are the same).

Table 3.3 Comparison of the fabricated prototypes with different platform-mounted antennas reported in the literature.

Ref	Appl.	$\frac{BW}{BW_{Chu}}$	CE No.	CE type	Cut Plat.	CE D[a]	Sys. D[a]
[81]	Handset	8.25%	1	Capacitive	Yes	0.29λ	0.43λ
	Handset	4.33%	1	Capacitive	Yes	0.14λ	0.42λ
[82]	Handset	5.75%	1	Capacitive	No	0.23λ	0.72λ
[38]	Military	0.19%	2	Inductive	Yes	0.54λ	3.73λ
[39]	Military	1.02%	2+1	Inductive	No	0.18λ, 0.22λ	1.03λ
This work							
–	Military	2.29%	1	Inductive	No	0.14λ	0.35λ
–	Military	5.30%	2	Inductive	No	0.13λ	0.32λ
–	Military	15.11%	4	Inductive	No	0.13λ	0.32λ

[a] Maximum linear dimension of the coupling elements or the system (coupling elements and platform) in terms of the wavelength.

printed structures were covered with copper tape. The feed networks for the scaled versions were etched on 0.02" thick Rogers RT/duroid 5880 substrates, as shown in Figs. 3.9(a)-3.9(c). To excite the multiple half loop antennas on the same platform with the same magnitudes and phases, a two-way power splitter (Mini-Circuits SP-2C1+) and a four-way power splitter (Mini-Circuits SCA-4-10+) were used. The realistic 2-1 and 4-1 power splitters have typical insertion losses of 0.4 dB and 1.2 dB, respectively. Figs. 3.9(d)-3.9(f) show photographs of the fabricated prototypes. The dimensions of the fabricated scaled models are provided in the caption of Fig. 3.9. The radiation parameters of the fabricated prototypes were measured using a multi-probe spherical near field system. The measured maximum directivity of the scaled versions of the one, two, and four half loop antennas are 4.2 dBi, 3.5 dBi, and 3.9 dBi, respectively. Fig. 3.10 shows the measured S_{11} of the fabricated prototypes. The measured 10 dB return loss fractional bandwidth of the one, two, and four half loop antennas on the platform are 0.91%, 1.78%, and 5.12%, respectively, as shown in Fig. 3.10 and Table 3.2. A relatively good agreement between the measured bandwidths of the scaled antennas and the simulated bandwidths of the full-scale antennas can be observed (see Table 3.1 and Table 3.2). The normalized radiation patterns of the antennas are also measured and shown in Fig. 3.11. From Figs. 3.2(a) and 3.11(c), it can be observed that the radiation patterns of the four half loop case are very much similar to those of the mode 1 of the platform: omni-directional in the $x-z$ plane, and figure-eight shaped in the $y-z$ plane. The minor differences between the radiation patterns of the fabricated prototype and those of mode 1 are primarily due to the presence of a large feeding cable, connected to the SMA connector on the bottom of the antenna, in the near field of the structure during measurement. Other factors contributing to these minor differences include tolerances in the fabrication and the possible small phase/amplitude imbalances between the different ports of the realistic power splitters used in the measurement process.

The radiation efficiencies of the one, two, and four loop antennas on the platform are 26%, 37%, and 32%, respectively. These low efficiency values are caused by two principal factors. The first one is the losses of the power splitters and the feed networks. The second source is the losses of the impedance matching networks of each individual loop. The matching network for any small antenna with a highly reactive input impedance (similar to the coupling loops used here) needs to cancel out a large reactance and match the antenna to 50Ω. If the VSWR of the unmatched antenna is very high, the intrinsic losses of the elements used in the impedance matching network are significantly magnified, resulting in a much larger realized loss, L_a, which can be calculated using [47]:

$$L_a = \frac{(\text{VSWR}+1)^2 L^2 - (\text{VSWR}-1)^2}{4L \cdot \text{VSWR}} \tag{3.9}$$

where L is the intrinsic loss of the impedance matching network in linear scale and VSWR is the voltage standing wave ratio for the unmatched antenna. Despite this enhanced loss, the total efficiencies of the different antennas examined in this work are quite similar to each other and fall in the range of $\approx 31\% \pm 5\%$. These relatively small differences between the efficiencies of these antennas are not significant enough to explain the significant differences in their measured bandwidths. The results presented in Fig. 3.10 and Table 3.2 demonstrate the validity of using the proposed technique in designing platform-mounted HF antennas with enhanced bandwidth. The total efficiencies of full-scale devices are expected to be higher than those of the scaled-model versions fabricated in this work. This is due to the fact that power dividers available at HF band have significantly lower loss values and the quality factors of the capacitors and inductors available at HF band (for impedance matching) are higher than those available at UHF band.

Table 3.3 compares the measured performances of the antennas proposed in this work with a number of other antennas that use the platform as the radiating element. While performing an exhaustive comparison is beyond the scope of this article, several representative examples reported very recently were chosen for this purpose. They include antennas designed for mobile handsets as well as those designed for military platforms. The table shows the ratio of the measured 10 dB return loss fractional bandwidth of each antenna to the maximum theoretical bandwidth achievable based on the Chu-McLean limit. Additionally, the number and types of coupling elements used, their maximum linear dimensions, and the maximum linear dimension of the system (coupling elements and platform) are also provided. The reported data suggests that as the electrical dimensions of the system and those of the coupling element increase, wider bandwidths can be achieved. Additionally, if the platform can be cut, additional modes may be created that can significantly increase the bandwidth (e.g. handset antenna reported in [81]). Cutting the platform has also been used in [38] to excite the desired modes. However, in the application examined in this work, cutting the platform is not an option. Nevertheless, the data presented in Table 3.3 shows that our proposed technique can be used to significantly increase the BW/BW_{Chu} ratio using relatively small coupling elements (in a military platform whose maximum linear dimension is less than $\lambda/2$) without needing to cut the platform.

Table 3.3 also shows that the system volume is used more efficiently when the number of our coupling loops increases. The bandwidth enhancement factor, however, will eventually saturate due to the increasing mutual coupling between the loops. Therefore, it is anticipated that an optimum number of coupling loops exists that, when arranged properly, can provide the bandwidth closest to the maximum available bandwidth. While determining this optimum configuration is beyond the scope of this paper, we studied a full-scale structure using eight half loops. This arrangement was found to provide a bandwidth of 4.17%, which indicates that some additional gains in bandwidth can be achieved

by increasing the number of loops. However, to achieve this additional 0.9% increase in bandwidth, four new coupling loops had to be added to the platform, which drastically increases the complexity of the system. Therefore, it appears to us that using four coupling loops provides a good compromise between enhanced bandwidth and complexity of the system.

In addition to the scaled versions of the scenarios shown in Fig. 3.5, we also examined several alternative structures that use multiple coupling loops. Specifically, we examined placing three half loops on the top of the platform, two half loops on the top and one half loop on each side of the platform, as well as one half loop on the centers of the top, the bottom, and the two sides as shown in Fig. 3.12. The feed networks used to feed each prototype are shown in Figs. 3.12(a)-3.12(c). The prototypes of these structures were also fabricated and characterized as discussed in the previous paragraph and are shown in Figs. 3.12(d)-3.12(f). The feed networks use three-way (Mini-Circuits SCA-3-11+) and four-way (Mini-Circuits SCA-4-10+) power splitters to excite the loops with the same magnitudes and phases. The realistic 3-1 and 4-1 power splitters have a typical insertion loss of 0.7 dB and 1.2 dB, respectively. The measured fractional bandwidth of the three half loops (Edge & Center) shown in Fig. 3.12(a), four half loops (Edge & Center) shown in Fig. 3.12(b), and four half loops (Center) shown in Fig. 3.12(c) are 1.97%, 2.84%, and 3.75%, respectively. The radiation efficiencies of these antenna systems are respectively 33%, 30%, and 26%. Comparison of the results shown in Table 3.2 demonstrates that the bandwidth of these antenna systems can be enhanced by distributing the coupling loops over the entire surface of the platform. Moreover, for the cases that a similar number of coupling loops are used, placing the loops at locations where the current density of the desired mode is strongest improves the bandwidth of the system. This is clearly seen by examining the performances of the antennas shown in Figs. 3.9(f) and 3.12(f). In both examples, four coupling loops and the same type of power divider are used. However, the

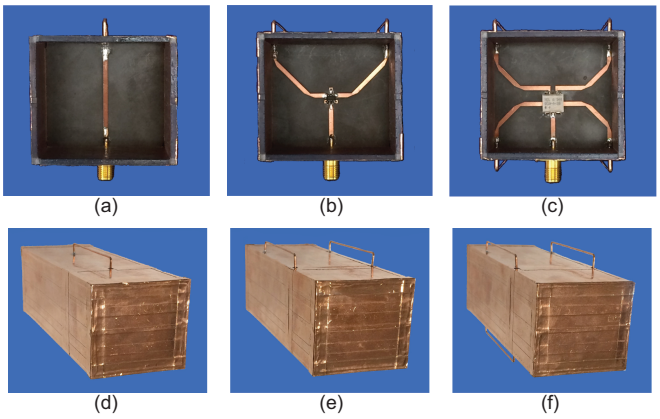

Figure 3.9 Photograph of the scaled platform-mounted antennas. One half loop scenario (Center): (a) feed network (d) prototype; Two half loop scenario (Edge): (b) feed network (e) prototype; Four half loop scenario (Edge): (c) feed network (f) prototype. The dimensions of the scaled platforms are 46.25 mm $\times$ 133.75 mm $\times$ 41.25 mm. The dimensions of the scaled half loops are 58.75 mm $\times$ 6.25 mm. The values of the capacitors for the one, two and four half loop scenarios are 0.25 pF, 0.4 pF and 0.4 pF, respectively.

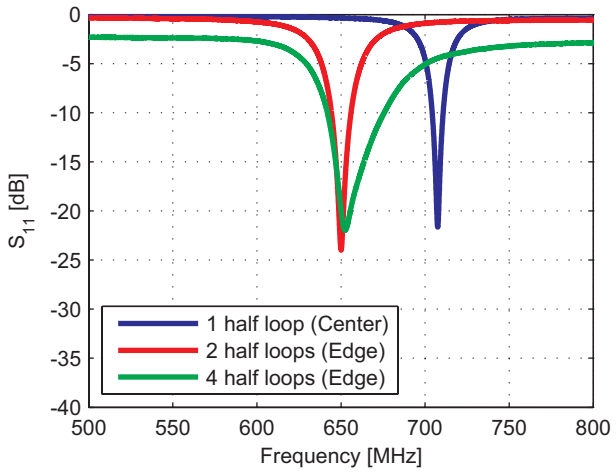

Figure 3.10 Measured S_{11} of the scaled platform-mounted antennas for one half loop antenna on the platform (Center), two half loop antennas on the platform (Edge), and four half loop antennas on the platform (Edge), as shown in Fig. 3.9.

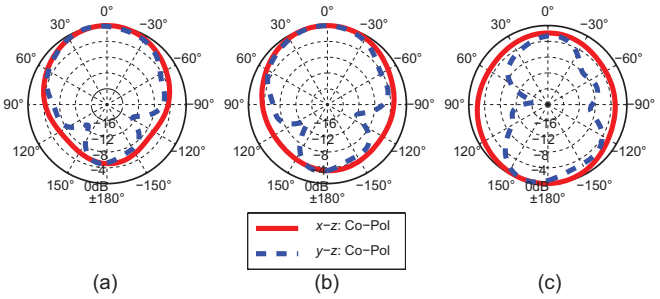

Figure 3.11 Measurement results of normalized radiation patterns (realized gain) of the scaled platform-mounted antennas on the $x-z$ and $y-z$ planes for (a) one half loop antenna on the platform (Center), (b) two half loop antennas on the platform (Edge), and (c) four half loop antennas on the platform (Edge), as shown in Fig. 3.9.

structure shown in Fig. 3.9(f) has a fractional bandwidth of 5.12% while the one shown in Fig. 3.12(f) has a fractional bandwidth of 3.75%. In addition to having a significantly wider bandwidth, the antenna shown in Fig. 3.9(f) has a slightly higher efficiency than the one shown in Fig. 3.12(e). The comparison of these two measurement results is further evidence that the proper placement of the antennas on the platform can significantly influence the bandwidth of the system and that the bandwidth gains are not due to the differences in efficiencies. In all cases, the radiation patterns are horizontally polarized and the direction of maximum radiation is orthogonal to the y axis of the platform. The maximum directivity values of the antennas are respectively 3.8 dBi, 2.8 dBi, and 3.1 dBi for the structures shown in Figs. 3.12(d), 3.12(e), and 3.12(f).

3.1.4 Applying the Proposed Approach to a More Realistic Platform

To demonstrate the applicability of the proposed approach to a more realistic platform, we applied the same design concepts to the U.S. Marine Corps Expeditionary Fighting Vehicle [87]. To do that, a simplified model of the EFV (Fig. 3.14(a)) was used in conjunction with full-wave EM simulations in FEKO. Fig. 3.13 shows the current distributions associated with the first few modes of this platform as well as their modal significances. As can be observed, the first four modes of this realistic platform are similar to those of the simplified platform shown in Fig. 3.2. Specifically, in the EFV model, mode 1 of the platform is the dominant mode and it is significant above approximately 11 MHz. When excited in this mode, the entire platform acts as a horizontally-polarized dipole antenna with an electric current oriented along the $\hat{y}$ direction. To excite mode 1 on the EFV, coupling loops can be placed on its surface according to the scenarios shown in Figs. 3.14(b)-3.14(f). In this case, we assume that the coupling loops are placed only on the top and the two side surfaces of the platform. Additionally, we considered placing up to four half loops on the surface of the platform in various configurations as shown in Fig. 3.14. Specifically, the

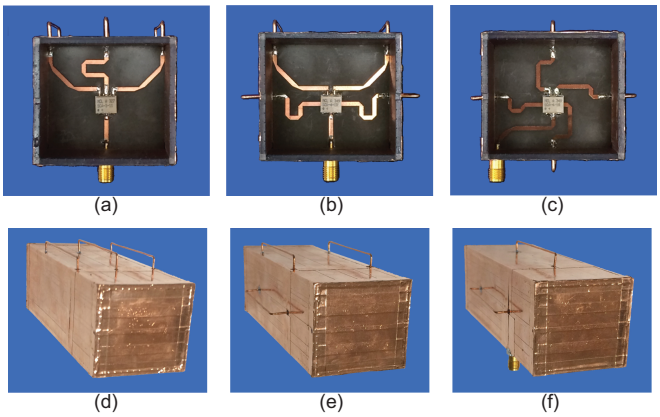

Figure 3.12 Photograph of the scaled platform-mounted antennas. Three half loop scenario (Edge & Center): (a) feed network (d) prototype; Four half loop scenario (Edge & Center): (b) feed network (e) prototype; Four half loop scenario (Center): (c) feed network (f) prototype. The dimensions of the scaled platforms are 46.25 mm $\times$ 133.75 mm $\times$ 41.25 mm. The dimensions of the scaled half loops in these scenarios are: (d) 58.75 mm $\times$ 7.75 mm (Center) and 58.75 mm $\times$ 6.25 mm (Edge); (e) 58.75 mm $\times$ 6.25 mm (Edge) and 58.75 mm $\times$ 8.55 mm (Center); (f) 58.75 mm $\times$ 6.4 mm (Center, Top & Bottom) and 58.75 mm $\times$ 6.25 mm (Center, Sides). The values of the capacitors in these scenarios are: (d) 0.3 pF (Center) and 0.35 pF (Edge); (e) 0.4 pF (Edge) and 0.35 pF (Center); (f) 0.25 pF (Center).

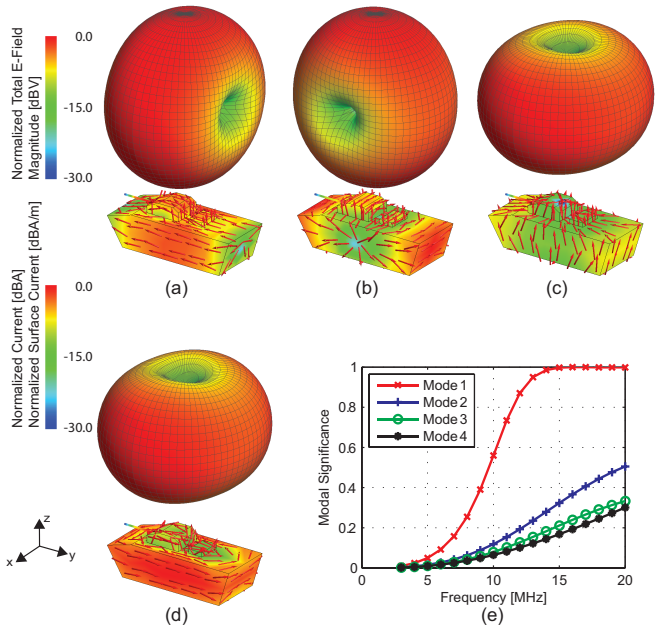

Figure 3.13 Simulated normalized current distribution and radiation patterns of the first four characteristic modes of the simplified EFV platform: (a) mode 1, (b) mode 2, (c) mode 3, and (d) mode 4. (e) Simulated modal significance of the simplified EFV platform.

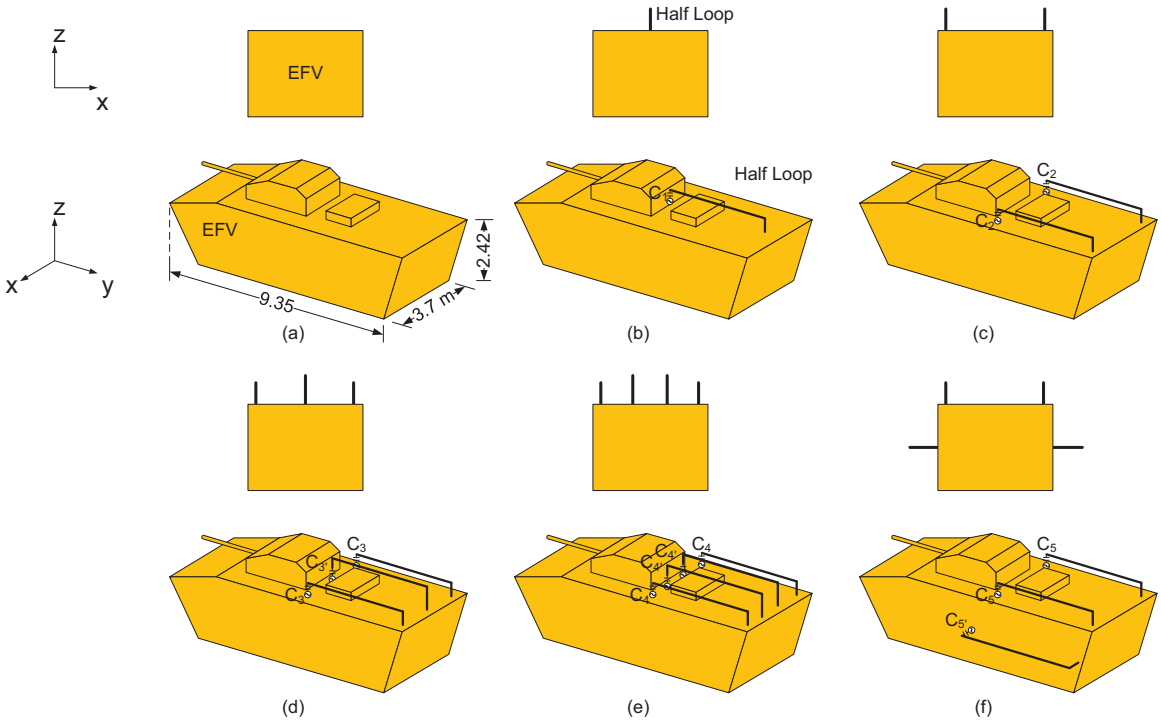

Figure 3.14 (a) The simplified EFV platform. (b) One half loop antenna (Top), (c) two half loop antennas (Top), (d) three half loop antennas (Top), and (e) four half loop antennas on the top of the simplified EFV platform (Top). (f) Two half loop antennas on the top and one half loop antenna on each side of the simplified EFV platform (Top & Side).

EFV model was examined when one, two, three, and four half loops were placed on the top surface of this platform as shown in Figs. 3.14(b)-3.14(e). Another topology, where two half loops are placed on the top and one half loop on each side of the platform (i.e. four half loops (Top & Side)), as shown in Fig. 3.14(f), was also considered. In the scenarios shown in Figs. 3.14(d)-3.14(e), the height of the half loop placed at the center on the top of the platform was tuned to match the operating frequency of the outer two half loops. Similarly, in Fig. 3.14(f), the length of the half loops on the side of the platform was tuned to match the operating frequency of the other two half loops. The particular topologies were chosen for practical reasons. The simulated S_{11} of the different cases are shown in Fig. 3.15. The S_{11} of the antennas are obtained by FEKO simulations that include the feed loops, the EFV, and the related ideal power splitters. Table 3.4 presents the simulated bandwidth of the different topologies. The bandwidth increases as the number of coupling loops increases, except the four half loops (Top) scenario. The fractional bandwidth of the four half loops (Top) scenario is less than that of the three half loops (Top) scenario because the strong mutual coupling between the four half loops increases the input impedance, which decreases the bandwidth. In the two arrangements shown in Figs. 3.14(e) and 3.14(f) where four feed loops are used, the fractional bandwidth of the antenna system of Fig. 3.14(f) is wider (3.85% vs. 3.36%). This is due to the fact that the distribution of the coupling loops along the periphery of the EFV more efficiently excites mode 1 of the platform compared to the case shown in Fig. 3.14(e). The simulated radiation patterns and current distributions of these antenna systems are shown in Fig. 3.16. Observe that, in all cases, the radiation patterns of the antenna systems show a direction of maximum radiation towards zenith and are horizontally polarized. As can be observed from the results shown in this section, this more realistic platform exhibits the same trends as the one demonstrated in Section 3.1.2 for a simplified platform through simulations and scaled-model measurements.

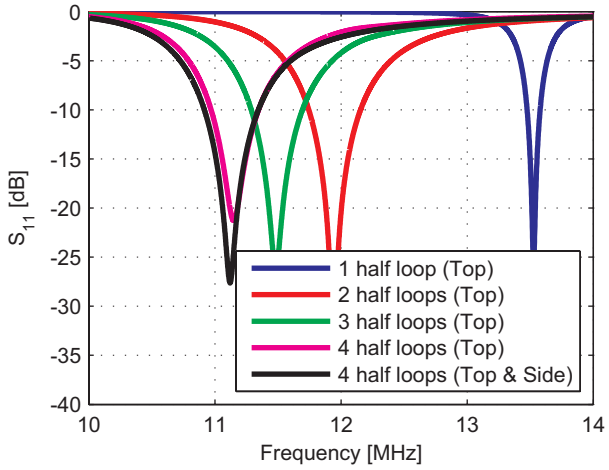

Figure 3.15 Simulated S_{11} of the EFV-mounted antennas, as shown in Fig. 3.14.

Table 3.4 Comparison of simulation results of the different antennas on the simplified EFV platform.

Scenario	f_0 (MHz)	BW
One half loop (Top)	13.53	0.75%
Two half loops (Top)	11.94	3.42%
Three half loops (Top)	11.48	3.52%
Four half loops (Top)	11.15	3.36%
Four half loops (Top & Side)	11.12	3.85%

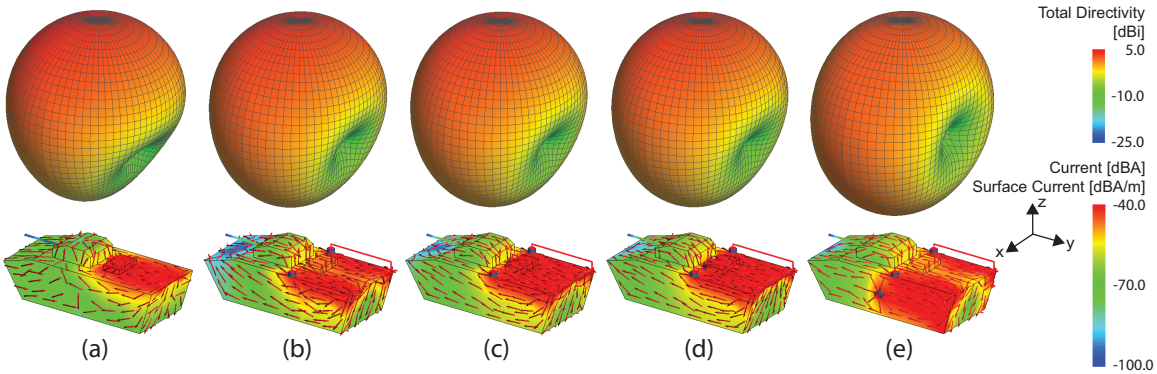

Figure 3.16 Simulated normalized current distributions and radiation patterns of the platform-mounted antennas, as shown in Fig. 3.14.

3.1.5 Conclusions

The results presented in this paper validate that excitation of the characteristic modes of a large platform can be used as a method for enhancing the bandwidth of platform-mounted HF antennas. A systematic method for designing platform-mounted antennas that can take full advantage of the presence of the platform was presented. In the example examined in this paper, a large rectangular-shaped box platform acts as the main radiator, and one or more small loop antennas are used to couple energy from a source to the desired resonant mode of the platform. It was demonstrated that the desired resonant mode of the platform can be successfully excited and that the bandwidth of this platform-mounted antenna can be enhanced by a factor of 2, 7, or 10 compared to one stand-alone full loop antenna by using one, two, or four half loop antennas to excite the desired mode. This is despite the fact that the maximum linear dimensions of the structure (feeding loops and the platform) are not changed. This bandwidth enhancement is due to the fact that, as the number of antennas is increased, the current distribution excited on the platform more closely resembles that of the desired mode. Scaled models were fabricated. The measured fractional bandwidth of the one, two, and four half loop antennas on the platform are 0.91%, 1.78%, and 5.12%, respectively. The upper limit of the 10 dB return loss fractional bandwidth that can be achieved from this approach was calculated to be 7.69% based on the Q of mode 1 of the platform. Three additional topologies with the measured fractional bandwidth of 1.97% (three half loops (Edge & Center)), 2.84% (four half loops (Edge & Center)), and 3.75% (four half loops (Center)) were presented to demonstrate the flexibility of this approach and examine the impact of the proper positioning of the loops to enhance the bandwidth. The proposed method was also applied to a realistic armored personnel carrier model. For practical reasons, the coupling loops cannot be placed on the bottom of this platform. To obtain a better approximation to a uniform magnetic current distribution

that encloses the entire platform, it is preferable to place the coupling loops on both the top and the sides of the platform at the edges. The distance between any two coupling loops was considered to prevent strong mutual coupling that increases the reactive part of the input impedance of the loops and decreases the bandwidth. Despite the fact that the bandwidth increases with the size of the loops, the dimensions of the coupling loops were restricted to 0.5 m in height to maintain a low profile. The excitation of the desired platform mode with up to four coupling loops was shown to result in a fractional bandwidth of up to 3.85%, which is more than sufficient to address many of the emerging needs of the wideband HF communications systems.

3.2 Design of Vehicle-Mounted, Compact VHF Antennas Using Characteristic Mode Theory

Compact and low-profile VHF antennas with enhanced bandwidth have a wide spectrum of applications in both commercial and military communication systems. Having both of these criteria in a single antenna, however, is very challenging. In this paper, we demonstrate a method for bandwidth enhancement of vehicle-mounted electrically-small antennas operating in the VHF band. In this method, the vehicle platform is considered to be the major part of the radiating structure, while a meandered monopole antenna is used as a capacitive coupling element to excite a desired set of characteristic modes of the platform. The size of the coupling element is $0.06\lambda \times 0.06\lambda \times 0.06\lambda$, where λ is the free-space wavelength at the frequency of operation, 60 MHz ($ka \approx 0.47$). The proposed approach was employed to successfully enhance the bandwidth of a vehicle-mounted VHF antennas by at least 400%.

3.2.1 Introduction

The very high frequency band (VHF, 30-300 MHz) is used for a wide range of applications including land mobile systems, TV and radio broadcasting or reception, and military and law-enforcement communication systems. Antennas used at these frequencies tend to be physically large due to the large wavelength of electromagnetic waves at these frequencies. This problem is more exacerbated if the antenna needs to cover very wide bandwidths, since even very compact ultrawideband (UWB) antennas can have relatively large physical dimensions at these wavelengths [94]. However, in applications where these antennas are to be mounted on a vehicular platform, it is desirable to reduce their physical dimensions as much as possible. Due to the large wavelength of the electromagnetic waves at these bands, the need for reduction of the antenna size often results in the use of electrically-small antennas (ESAs). A common characteristic of an ESA is its small radiation resistance and large reactance. These result in reduction of the antenna efficiency and its bandwidth [2].

In many modern applications, ESAs are installed on metallic platforms that are significantly larger than the antennas themselves. To enhance the bandwidth of such an ESA, or any antenna that is mounted on a platform with limited space to accommodate it, one promising approach is to exploit the presence of the platform as a major part of the radiator. This concept has been previously used in a number of applications including designing antennas for mobile terminals [81]– [82] and skywave HF communication systems [95]. In most of these studies, however, the platform was cut to allow for the excitation of the desired platform mode(s), which is often not practical. We have recently developed a method to fully excite a single platform mode to enhance the bandwidth of a platform-mounted antenna while keeping the platform intact [95]. In this method, multiple coupling elements are located on the periphery of the platform and are excited in phase to excite the

desired platform mode as efficiently as possible. In this method, bandwidth enhancement was achieved by efficiently exciting the dominant mode of the platform using a plurality of coupling elements. An alternative way of increasing the bandwidth of a platform mounted antenna using characteristic modes of the platform is to partially excite multiple platform modes at once. This has the added advantage of reducing the number of coupling elements needed to achieve a given antenna bandwidth. In this paper, we demonstrate how the bandwidth of platform-mounted antennas can be improved by simultaneously exciting a combination of selected characteristic modes of the platform.

3.2.2 Antenna Design

To demonstrate the use of this method, we consider a simplified model for a typical light armored vehicle, the High Mobility Multipurpose Wheeled Vehicle (HMMWV), commonly known as the Humvee, as our platform. To expedite the design process, the Humvee platform was simplified as shown in Fig. 3.17(a) and the entire structure is assumed to be made out of metal, except of the tires (highlighted in black). This vehicle will be treated as part of the antenna and will act as the main radiating structure. Thereby, the maximum linear dimension of the antenna system can be increased significantly, which is expected to result in an enhanced bandwidth for the antenna.

The design process starts by examining the characteristic modes of the platform. The commercial full-wave simulation software FEKO was used to perform the analysis of characteristic modes. Fig. 3.17(b) shows the modal significance curves of the first four characteristic modes[2] of the simplified Humvee. When the modal significance of a mode attains a value of 0.707, it is considered as significant. Considering an operating frequency of 60 MHz, all of the first four modes of this platform are significant, as can be observed from

[2]FEKO numbers the characteristic modes according to their modal significance values and from low frequency to high frequency.

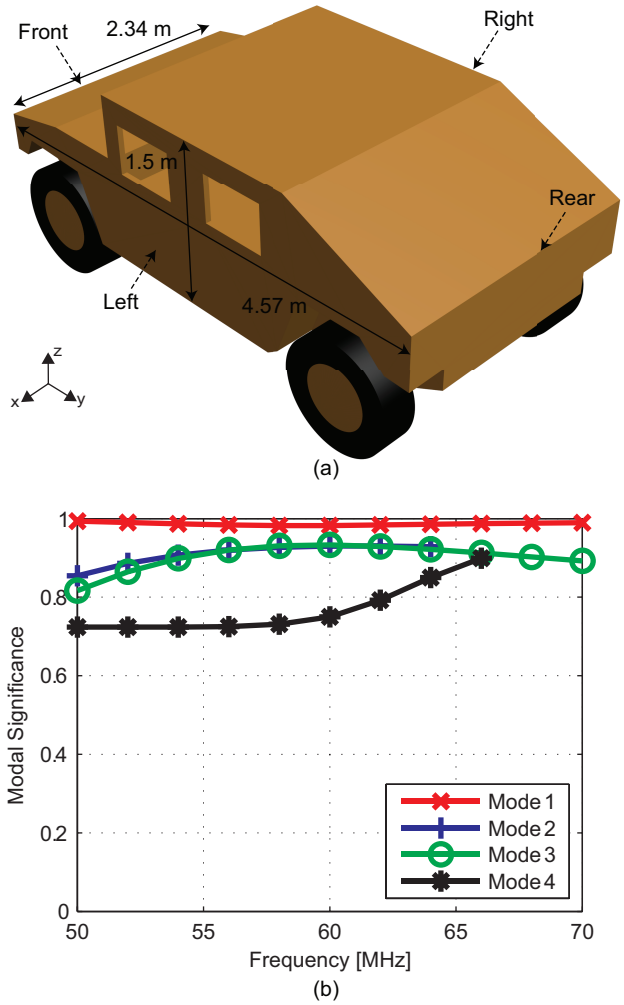

Figure 3.17 (a) The simplified model of a Humvee. (b) Simulated modal significances of the first four characteristic modes of the simplified Humvee.

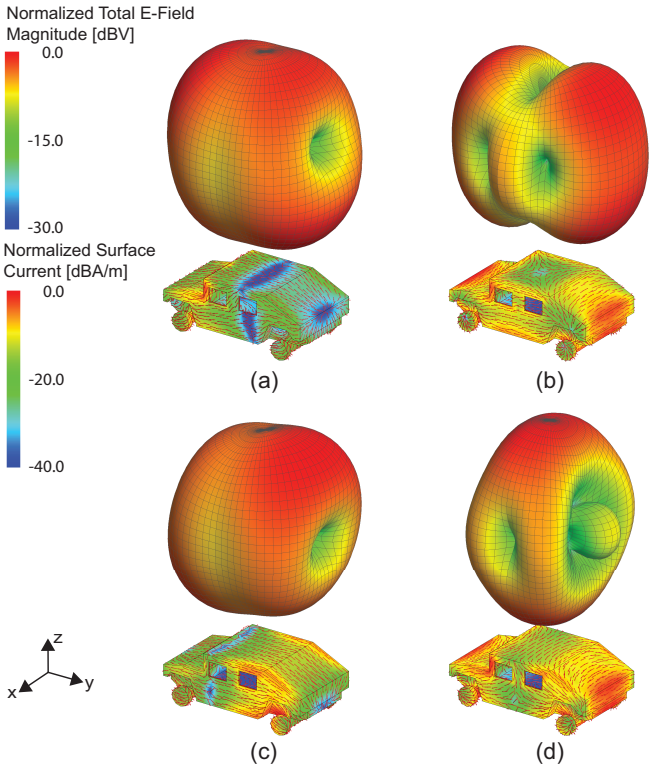

Figure 3.18 Simulated normalized current distributions and normalized radiation patterns of the first four characteristic modes of the simplified Humvee. (a) Mode 1, (b) mode 2, (c) mode 3, and (d) mode 4.

Fig. 3.17(b). The electric current distributions and the radiation patterns of these modes are shown in Fig. 3.18. To excite individual characteristic modes of a platform, capacitive or inductive coupling techniques can be applied. Specifically, inductive coupling elements should be placed where the electric current density of the specific mode is the strongest, and capacitive coupling elements (CCEs) should be placed where the electric current density of the specific mode is the weakest. For example, from Fig. 3.18(a), it can be observed that the center of the rear edge of the trunk lid can be utilized to capacitively excite mode 1, whereas the left and right edges of the engine hood and windshield can be used to inductively excite the exact same mode. A closer examination of the currents of the modes shown in Figs. 3.18(a)-(d) reveals that the front and rear corners of the simplified Humvee can be used to capacitively excite all of the first four modes of this platform. More importantly, this can be done without cutting the platform. In this work, the left upper rear corner is used as the location for placement of the capacitive coupling element. To demonstrate our method, a meandered monopole antenna (acting as a CCE) is placed at this corner to couple energy from the source and to excite the desired modes, as shown in Fig. 3.19. The particular topology was chosen for practical reasons. If the antenna were mounted on the front part of the the vehicle, it would become more suspectable to damage and might interfere with the installation of illumination units. The proposed antenna is made from meandered sections to reduce the maximum linear dimension of this coupling element. The size of the CCE is $0.06\lambda \times 0.06\lambda \times 0.06\lambda$, where λ is the free-space wavelength at the frequency of operation, 60 MHz, corresponding to a $ka \approx 0.47$. k is the wavenumber and $a = 37.78$ cm is the radius of the Chu sphere containing the coupling element. The diameter of the monopole wire is 1.27 cm. To match the input impedance, a two-element LC matching network is placed between the excitation source and the antenna.

Fig. 3.20 shows a comparison of the input reflection coefficients of the antenna placed on an infinite ground plane and the antenna operating at the left upper rear corner of the

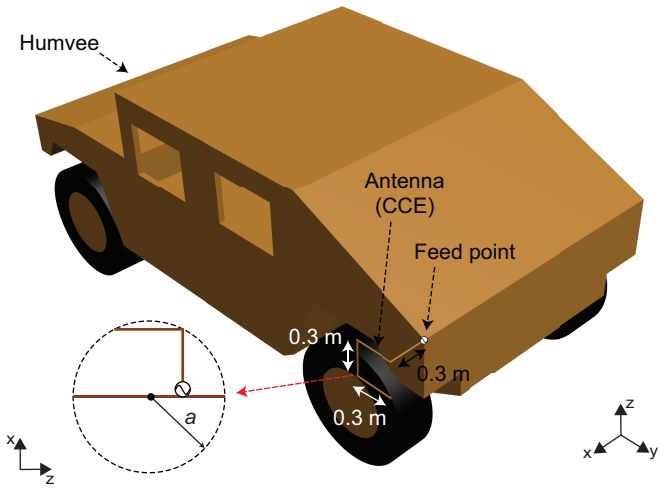

Figure 3.19 The meandered ESA is placed on the left upper rear corner of the simplified Humvee to excite multiple characteristic modes of the platform. The diameter of the monopole wire is 1.27 cm. $a = 37.78$ cm is the radius of the Chu sphere containing the coupling element.

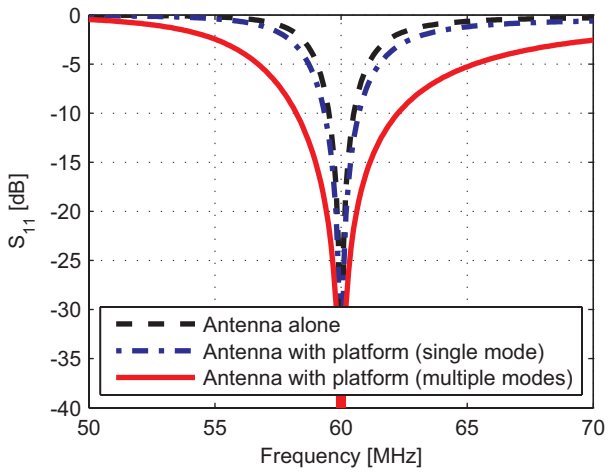

Figure 3.20 Simulated S_{11} of the antenna when placed on an infinite ground and when used to excite a single mode or multiple modes of the simplified Humvee.

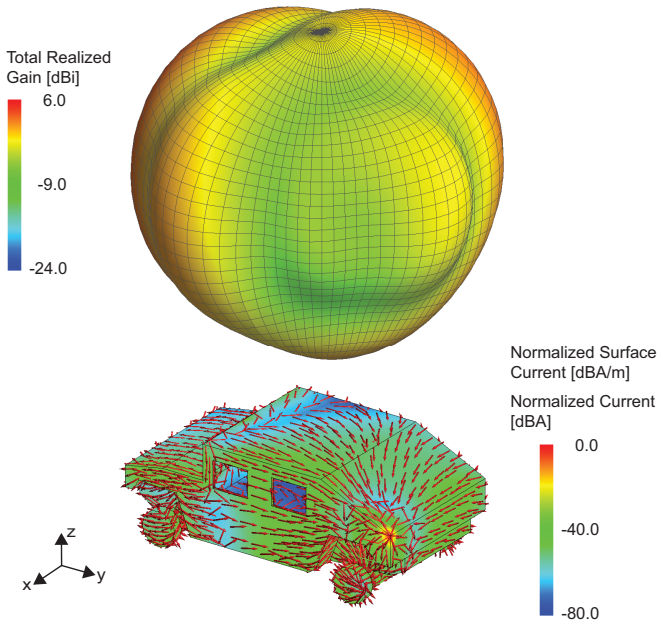

Figure 3.21 Simulated normalized current distribution and radiation pattern of the antenna mounted on the simplified Humvee.

simplified Humvee. The simulation was conducted in FEKO. As can be observed, the Humvee-mounted antenna exhibits a bandwidth four times that of the one placed on the infinite ground plane (6.72% compared to 1.65%). Relocation of the antenna to the center of the rear trunk lid edge for mode 1 excitation results in a bandwidth of 2.27%. The simulated current distribution excited on the simplified Humvee and the radiation pattern of the combined modes are shown in Fig. 3.21.

3.2.3 Conclusions

The results presented in this paper show that improving the bandwidth of electrically-small antennas mounted on a vehicular platform can be achieved by simultaneous excitation of more than one characteristic mode of the platform. In the example examined in this paper, a High Mobility Multipurpose Wheeled Vehicle (i.e. Humvee) acts as the main radiator and a meandered monopole antenna is used to couple energy from a source and to excite the desired set of characteristic modes of the platform. It was demonstrated that the bandwidth of this antenna could be enhanced by a factor of four when utilizing the selected characteristic modes of the vehicle compared to the antenna operating in isolation (6.72% compared to 1.65%). This was achieved without cutting the platform. Moreover, if the same antenna had been used to excite only a single characteristic mode of the platform, the bandwidth would be 2.27%. This indicates that excitation of multiple modes at the same time allows for improving the bandwidth of the antenna without increasing the number of required excitation elements.

As described in the previous section, different types of coupling elements can be used to excite the same set of characteristic modes. We are currently investigating the impact of the use of inductive and capacitive coupling elements. Another direction that we are working on is to systematically determine the optimum location for placing the antennas to maximize the coupling efficiency with which the desired modes are excited. We are also

examining the possibility of further bandwidth improvement by adding magnetic materials to the coupling elements to improve the coupling efficiency between the antenna and the platform. Details of these additional investigations as well as the measurement results of fabricated prototypes of scaled versions of these antennas will be presented and discussed at the symposium.

Chapter 4

High-Efficiency Wideband Non-Foster Matching Circuit for Electrically-Small Transmitting Antennas

4.1 Using Non-Foster Circuits

Due to the small radiation resistances and large reactances of electrically-small antennas (ESAs), passive impedance matching of these antennas can be performed only over very narrow bandwidths and the resulting antennas will have low gains. In this paper, we present a new non-Foster transmit matching architecture for electrically-small monopole antennas that achieves wide bandwidth, high transmission efficiency (transducer power gain), and stability at the same time. The measured 6 dB return loss fractional bandwidth of the proposed non-Foster transmitting system is 110% (c.f. 0.076% when the same electrically-small monopole antenna is matched with conventional Foster matching). The transmission efficiency (transducer power gain) of the system is improved by as much as 34.4 dB compared to the same antenna without the proposed non-Foster matching circuit, and it retains an enhanced transducer power gain over the entire frequency band of operation (26 MHz–89 MHz). The system remains stable within this frequency band.

4.1.1 Introduction

The high-frequency (HF) band (3-30 MHz) and the very high frequency (VHF) band (30-300 MHz) are used for various civilian and military applications including amateur radio, FM radio broadcasting, long-range data communication, and electronic warfare. Many antennas used at these frequencies tend to be electrically small due to the large wavelengths of the electromagnetic waves at these frequencies. Electrically-small antennas (ESAs) have very small radiation resistances and large reactances [1]– [19]. Consequently, they have very high radiation quality factors (Qs) and are difficult to match.

When matched with conventional passive circuits composed of positive valued capacitors or inductors (Foster circuits), ESAs suffer from narrow bandwidth or from low gain

due to the realizability constraints imposed by the gain-bandwidth limitation theory [21]–[23]. This is because positive valued capacitors or inductors are only capable of canceling out the reactance of an ESA at discrete frequencies. In theory, active non-Foster matching circuits produce lossless impedances with a negative reactance-to-frequency slope that allow for bypassing the gain-bandwidth limitations by canceling out the reactance of the ESA over a wide and continuous frequency band. This technique has been widely used in receiving ESA systems [40]– [44]. In 1968, the earliest application of non-Foster matching circuit to electrically-small receiving antennas was proposed [40]. The multistage transistor-based circuit in this work provides negative capacitance that is controlled by a voltage feedback loop. The advantage of using negative impedance matching circuits for receive ESAs was also stated. It improves received signal-to-noise ratio (SNR) only in those frequency ranges where receivers are internal-noise limited but not external-noise limited. This research was extended in [41] where the negative capacitance is realized using operational amplifiers. In [42], active coupling networks are used for electrically-small receiving antennas, but the inherent bandwidth and noise issues with solid state devices limited their use. The designs in [43] use transistor-based negative impedance converters (NICs, introduced by [45]) to generate negative capacitors or negative inductors to implement non-Foster circuits for receive antennas. A 9 dB SNR improvement was achieved at 30 MHz in an actual experiment. In [44], it was suggested that, with low-noise floor levels, a receiving system consisting of a passive ESA and an amplifier can provide better SNRs compared with a receiving system with a non-Foster matched ESA. On the other hand, little work has been published on non-Foster matching techniques for ESAs in transmit applications [43, 46]. Class A [46], class B [46], and class C [43] NICs[1] were

[1]Class A, class B, and class C circuits conduct 100%, 50%, and less than 50% of the input signal, respectively.

used for the same electrically-small monopole antenna model[2]. In the experiments in [46], the use of class A and class B NICs resulted in transducer power gain improvements compared to passive matching circuits that exceeded 20 dB in the lower part of the operating frequency band (15 MHz–30 MHz, 67% transducer power gain improvement bandwidth); while in [43], the class C NIC improved the transducer power gain by 10 dB at the center part of the operating frequency band (21 MHz–22.2 MHz, 6% transducer power gain improvement bandwidth). There are some additional challenges that must be overcome for designing transmit matching circuits for ESAs. First, the matching loss magnification must be overcome. Matching loss magnification reduced the transmission efficiency (low transducer power gain) between the source and the antenna because of the multiple reflections[3] that exist between a high Q ESA and its matching circuit [47]. Secondly, a non-Foster transmit antenna must be capable of handling very high voltage/current swings at the antenna terminals to allow for sufficient power transmission [43, 47]. Finally, in wideband non-Foster matching networks, circuit stability is another problem that has to be taken care of [43, 48].

The major source of loss in ESAs is the loss in the impedance matching networks. The matching network for an ESA, which is highly reactive, needs to cancel out the large reactance and match the input impedance of the antenna to 50 Ω. If the matching network is composed of lump elements (discrete inductors/capacitors), requirements for matching such a highly reactive antenna will produce very large circulating currents and/or high standing voltages (i.e. multiple reflections) between the antenna and the matching circuits. This magnifies the intrinsic matched loss to a much larger realized loss which results in low transmission efficiency [47]. Moreover, due to the small radiation resistance (R_r) and

[2]a series resonant RLC circuit: $R = 1\ \Omega$, $L = 1.8\ \mu$H, and $C = 33$ pF

[3]Under the high Q condition, a large circulating currents is generated between the antenna and the matching circuit. Similarly, large voltage standing waves are produced within the matching circuit.

large reactance (X_a) of the high Q ESA, only a small fraction of the applied voltage/current reaches the radiation resistance. Consequently, the matching circuit has to build up a very large voltage or current swing at the ESA terminal in exchange for even low radiated power. The stability of non-Foster transmitting systems is a another major concern due to the use of active components in these systems. It is very critical that the stability of these systems is ensured to avoid spurious radiation from the antennas. Addressing more than one of these challenges will be extremely difficult, but also a major breakthrough for electrically-small transmit applications, especially for those operating in the HF and lower VHF frequency bands (e.g. military communication systems, electronic warfare applications, etc.).

In this paper, we present a new non-Foster matching network for electrically-small monopole antennas in low-power transmit applications. The proposed antenna achieves wide bandwidth, high transducer power gain, and stability at the same time. The architecture of the proposed non-Foster matching circuit consists of a common-base amplifier, a transformer, and a negative impedance converter (NIC). In the example presented in this paper, this transmit circuit is used to match a 12.59" high monopole antenna (0.028λ at the lowest operating frequency, 26 MHz) that functions in the HF/VHF frequency band. Our experimental results show that the non-Foster transmitting system remains stable within the operating frequency band (26 MHz–89 MHz), and that the transmission efficiency (transducer power gain) of this system was successfully enhanced throughout this frequency band by up to as much as 34.4 dB using the proposed non-Foster circuit. The measured 6 dB return loss fractional bandwidth of this system is 110%, while the maximum bandwidth that can be achieved using passive matching for the same system is 0.076% at 26 MHz. The design concepts and the topology of the proposed non-Foster matching architecture are equally applicable to other non-Foster matching circuits for electrically-small monopole antennas used in transmit applications.

4.1.2 Electrically-Small Monopole Antenna

The antenna used in this work is a brass electrically-small monopole antenna (height: 12”; diameter: 0.5”). It is placed on a brass ground plane (size: 24”×24”; thickness: 0.016”) and probe-fed with a SMA (SubMiniature version A) connector (feed height: 0.59”). This antenna is designed for low-power transmit applications operating in the HF/VHF frequency band. The following subsections discuss the effects of the aforementioned challenges of transmit matching on this electrically-small monopole antenna.

4.1.2.1 Narrow Impedance Bandwidth

The simulated and measured real and imaginary parts of the input impedance of the employed electrically-small monopole antenna are shown in Fig. 4.1. The commercial software Altair FEKO was used to carry out the simulations. As can be observed, the monopole antenna has small radiation resistance and large reactance. In other words, it has a high quality factor (Q), and it can be modeled as an RC circuit. Performing passive matching for this antenna, like other ESAs, results in narrow impedance bandwidth or low gain due to the constraints imposed by the gain-bandwidth theory [21]– [23]. When matched with a passive matching network, the maximum available bandwidth of the passive matched antenna can be calculated as [2]– [19]:

$$B_V = \frac{1}{\eta}\frac{1}{Q}\frac{\text{VSWR}-1}{\sqrt{\text{VSWR}}} \tag{4.1}$$

$$Q = \frac{1}{ka} + \frac{1}{(ka)^3} \tag{4.2}$$

where Q is the quality factor, k is the wave number ($2\pi/\lambda$), a is the radius of the minimum size sphere that encloses the antenna, B_V is the upper bound of the matched VSWR fractional bandwidth, η is the radiation efficiency, and VSWR is the voltage standing wave

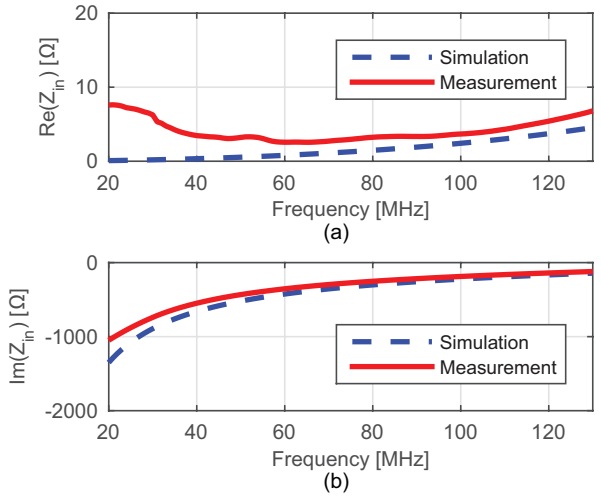

Figure 4.1 The simulated and measured (a) real part and (b) imaginary part of input impedance of the electrically-small monopole antenna.

ratio. For the electrically-small monopole antenna examined here, we have $a = 12.59" \approx 0.32$ m and $k = 2\pi/\lambda \approx 0.54$ at 26 MHz resulting in a quality factor $Q \approx 1523.34$. Assuming that $\eta = 100\%$ and VSWR $= 3.01$ (return loss is 6 dB), the upper bound of the matched fractional bandwidth is about 0.076%.

4.1.2.2 Low transmission efficiency

Matching circuits for ESAs are designed to cancel out the large reactance of the ESAs and transform the small input resistance of the ESAs (radiation resistance and loss resistance) to the value of system impedance (usually $50\ \Omega$ or $75\ \Omega$). Regardless of the matching scheme, passive or active, large circulating currents are generated flowing between the high Q ESA and its matching circuit. Likewise, large voltage standing waves are produced within the matching circuit. These multiple reflections magnify the intrinsic loss of the realistic components in a two-port matching network (L) to a much larger realized loss, L_A [47, pp. 46–48]:

$$\begin{aligned} L_A &= \frac{\text{power available from the source}}{\text{power delivered to the antenna}} = \frac{P_S}{P_{rad}} \\ &= \frac{(\text{VSWR}+1)^2 L^2 - (\text{VSWR}-1)^2}{4L \cdot \text{VSWR}} \end{aligned} \tag{4.3}$$

where L is the intrinsic loss of the impedance matching network in linear scale and VSWR is the voltage standing wave ratio for the unmatched antenna. For example, for our 12.59" high electrically-small monopole antenna, $VSWR$ is equal to 430 (83283) at 100 MHz (30 MHz). If the matching network has a loss of $L = 0.1$ dB, then L_A is 7.75 (29.82) dB at 100 MHz (30 MHz). This large realized loss results in low transmission efficiency, η_t, defined using:

$$\eta_t = \frac{\text{power delivered to the antenna}}{\text{power available from the source}} = \frac{P_{rad}}{P_S} \tag{4.4}$$

Another way to look at the low transmission efficiency is to examine the transducer power gain, G_T, defined as [96]:

$$\begin{aligned} G_T &= \frac{\text{power delivered to the load}}{\text{power available from the source}} = \frac{P_L}{P_S} \\ &= \frac{1-|\Gamma_S|^2}{1-|\Gamma_{IN}\Gamma_S|^2} |S'_{21}|^2 \frac{1-|\Gamma_L|^2}{1-|S'_{22}\Gamma_L|^2} \end{aligned} \tag{4.5}$$

$$\Gamma_{IN} = S'_{11} + \frac{S'_{12}S'_{21}\Gamma_L}{1-S'_{22}\Gamma_L} \tag{4.6}$$

where Γ_S is the reflection coefficient looking into the source, Γ_{IN} is the reflection coefficient looking into port 1 of the network, S'_{11} is the voltage reflection coefficient at the input terminal, Γ_L is the reflection coefficient looking into the load, and S'_{22} is the voltage reflection coefficient at the output terminal, as shown in Fig. 4.2. For an ESA matched with

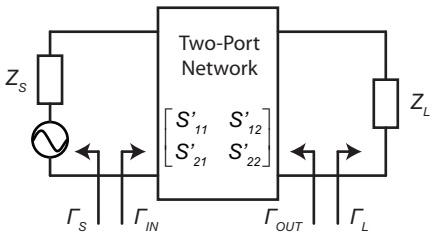

Figure 4.2 Generalized block diagram of a two-port network connected to arbitrary source and load terminations.

a two-port matching network, S'_{21} is the transmission coefficient of the matching network, Γ_L is the reflection coefficient of the ESA, and the source impedance is $50\ \Omega$ ($\Gamma_S = 0$). The transducer power gain of the matched antenna, G_{TA}, can be expressed as:

$$G_{TA} = |S'_{21}|^2(\frac{1-|\Gamma_L|^2}{1-|S'_{22}\Gamma_L|^2}) = \frac{P_L}{P_S} = \frac{P_{rad}}{P_S} = \eta_t. \tag{4.7}$$

As can be observed, the transmission efficiency (G_{TA}), is not only determined by the transmission coefficient of the matching work (S'_{21}) but also by the reflection coefficient of the antenna (Γ_L). Since the antenna is electrically small, its reflection coefficient is close to 1. Consequently, it will have low transmission efficiency.

4.1.2.3 High Voltage Swing Requirement

The voltage fed to electrically-small monopole antennas (V) is divided between the large capacitive reactance and the small resistance of the antenna:

$$V = I_A \times Z_A \tag{4.8}$$

$$\begin{aligned} Z_A &= R_A + jX_A \\ &= (R_l + R_r) + jX_A \end{aligned} \tag{4.9}$$

where I_A is the current flowing into the antenna, Z_A is the antenna impedance, R_A is the real part of Z_A, X_A is the imaginary part of Z_A, R_l is the loss resistance of the antenna,

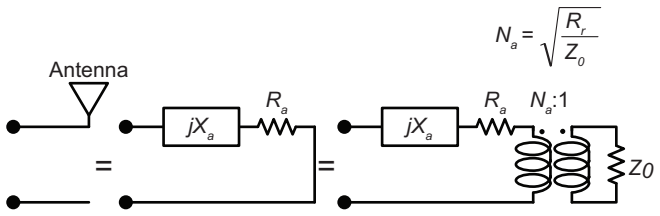

Figure 4.3 The two-port network model of the electrically-small monopole antenna.

and R_r is the radiation resistance. Due to the large antenna impedances composed of the small radiation resistances and large reactences, high Q monopole antennas require large RF voltages at the antenna terminals in order to radiate even low or moderate levels of power [43, 47]. In other words, the stored energy of these high Q antennas is much higher than their radiated energy. Therefore, in order to radiate the desired amount of energy, our electrically-small monopole antenna requires a high voltage swing that meets the much higher stored energy requirement. To incorporate the proposed antenna into system simulations and enable voltage calculations, the antenna is modeled as a two-port circuit, as shown in Fig. 4.3.

4.1.3 Non-Foster Transmit Matching Circuit Design

4.1.3.1 Background

Bipolar-junction-transistor-based negative impedance converters (BJT-NICs) are commonly used to implement non-Foster circuits due to their physical characteristics of transistors, their compactness, and their simple power requirement [45]. However, similar to the situation of passive matching circuits, multiple reflections are generated between these conventional non-Foster matching circuits and a high Q ESA. Therefore, most non-Foster matched ESAs reported to date suffer from low transmission efficiency, which is usually

less than 10% (-10 dB transducer power gain) [43]. To allow the ESA to radiate the desired amount of power, the non-Foster transmit matching circuits also have to create the required high voltage swing at the ESA's terminal. Moreover, the non-Foster impedance matching network must also be stable over the desired operating frequency. The non-Foster impedance matching network presented in this section addresses these challenges. The network consists of two parts. These include a voltage amplification section consisting of a common-base amplifier and an impedance matching section consisting of a transformer and a BJT-based negative impedance converter.

4.1.3.2 Voltage Amplification and Buffer Stage

To meet the high voltage requirement of the electrically-small monopole for transmit, one common way is the resonant load technique where an inductor is placed in conjunction with the antenna. However, this method results in small bandwidth (usually 5%-10%) [43]. Alternately, a common-base amplifier (also known as grounded base amplifier) can be used. A common-base amplifier is a basic single-stage amplifier (Fig. 4.4(a)), and it is typically used as a voltage amplifier or a current buffer. In the proposed circuit, a common-base amplifier is designed as the first stage to generate the voltage necessary for the desired radiated power transmission. The base of the proposed voltage amplifier is connected to the AC ground, as shown in Fig. 4.4(b)-(c), to prevent the formation of the multiple reflections between the matching circuit and the ESA which results in the matching loss magnification and the low transmission efficiency problems. In this configuration, this common-base amplifier provides a high isolation (S_{12}) between the matching circuit and the ESA. The high isolation also alleviates the system stability problem. The common-base amplifier is also designed to provide a small gain rather than a loss. Hence, there is no matching loss from the common-base amplifier itself that will be magnified.

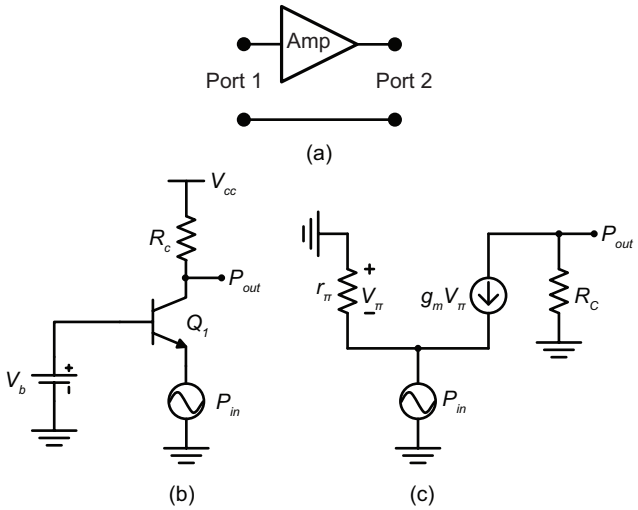

Figure 4.4 (a) A single stage amplifier. (b) The topology of the proposed common-base amplifier and (c) its small-signal model.

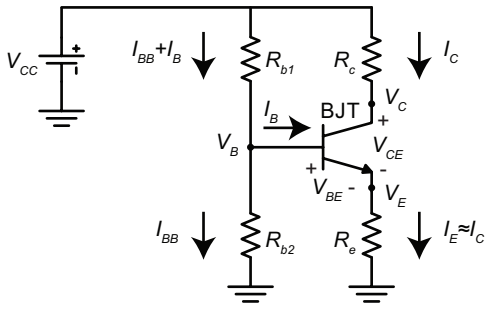

Figure 4.5 The schematic of a voltage divider bias circuit.

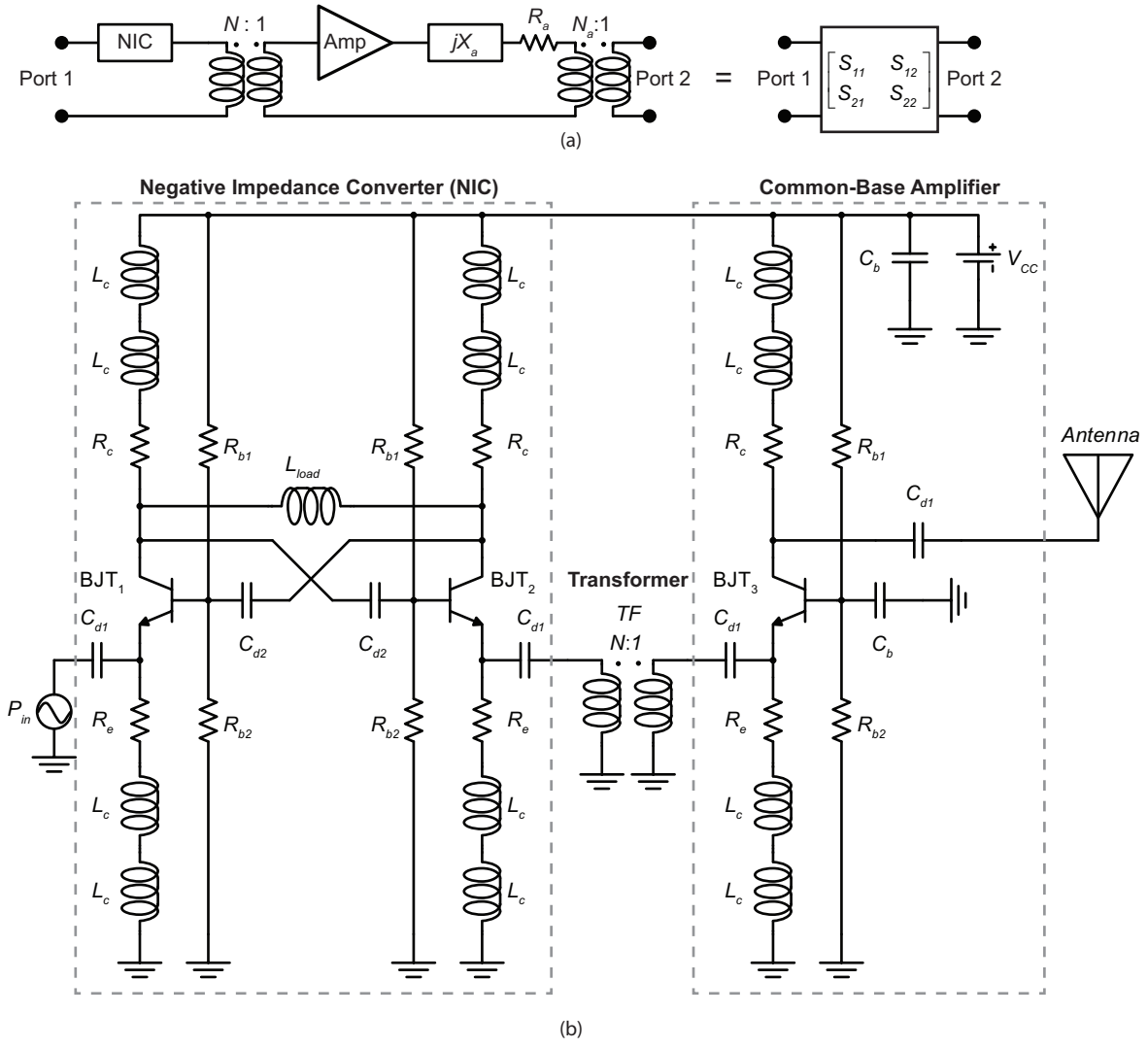

Figure 4.6 The (a) simplified and (2) complete schematic of the non-Foster transmitting matching circuit.

The proposed common-base amplifier circuit is composed of a transistor, a bias circuit (four resistors), RF chokes and DC blocks. The transistor used in our design is Infineon BFP-540ESD (typical $\beta = 110$), which is suitable for operating in the HF/VHF frequencies. The proposed amplifier must operate reliably and maintain its desirable characteristics (e.g. provide gain, amplify voltage) as temperature changes (due to changes in the environment as well as due to the heat generated by the active devices themselves). Therefore, the bias circuit has to be designed carefully. ΔV_{BE} and $\Delta\beta$ are two basic transistor characteristics that have significant effect on the transistor's DC operating point over temperature, and the goal of this bias circuit design is to minimize the effects of these parameters on the DC operating point of the transistors. To accomplish this, we use the voltage divider circuit shown in Fig. 4.5. To set the desired DC operating point for the transistor ($I_C = 40$ mA and $V_{CE} = 2.5$ V), the values used for the four resistors in the bias network are:

$$R_E = \frac{V_E}{I_E} \tag{4.10}$$

$$R_C = \frac{V_{CC} - V_C}{I_C} \tag{4.11}$$

$$R_{b1} = \frac{V_{CC} - V_B}{I_{BB} + I_B} \tag{4.12}$$

$$R_{b2} = \frac{V_B}{I_{BB}} \tag{4.13}$$

where V_E, V_B, and V_C are the voltages at the emitter, base, and collector, respectively; I_E, I_B, and I_C are the emitter, base, and collector currents, respectively; V_{CC} is the supply voltage (20 V in our case); and I_{BB} is the current flowing through R_{b2}. In our case, where $V_{CC} = 20$ V, $V_E = 10$ V and $I_{BB} = 0.2 \times I_C$, $R_{b1} = 1.1$ kΩ, $R_{b2} = 1.33$ kΩ, $R_e = 237\ \Omega$, and $R_c = 196\ \Omega$, as shown in Fig. 4.5(b). Note that these are the commercially

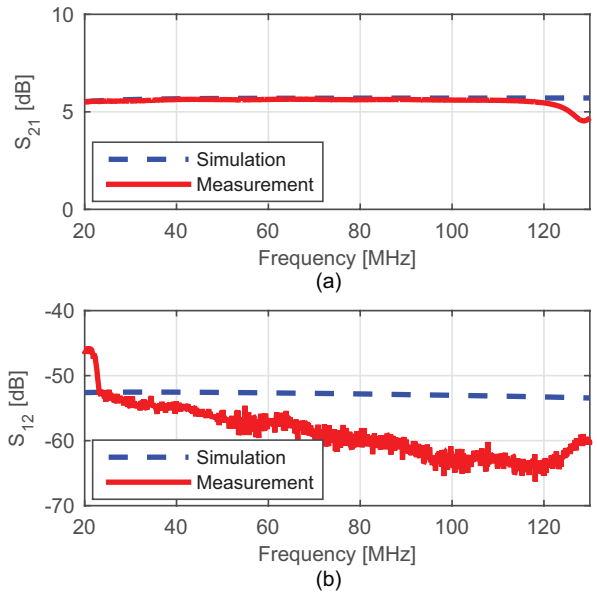

Figure 4.7 The (a) S_{21} and (b) S_{12} of the common-base amplifier circuit.

available values closest to the calculated results. The RF choke in the proposed common-base amplifier circuit is composed of two cascade inductors ($L_c = 2.7$ μH). The RF choke provides the required large impedance (> 1 kΩ) for RF signals within the operating frequency band, and its self-resonant frequency is above the operating frequency band of the non-Foster network. Capacitors ($C_{d1} = C_b = 47$ nF) are employed as DC blocks in the common-base amplifier. C_b also acts as a RF bypass capacitor. The detailed schematic of the proposed common-base amplifier is shown in Fig. 4.6. The simulated and measured S_{21} and S_{12} of this amplifier are shown in Figs. 4.7(a) and (b), respectively. As can be observed, the proposed common-base amplifier provides a measured S_{21} of 4.6 dB–5.7 dB and a 45.6 dB–66.3 dB isolation (-S_{12}) over the examined frequency band (20 MHz–130 MHz). A voltage gain ($|V_{out}|/|V_{in}|$) of 39.6–44.0 is provided by the proposed amplifier, as shown in Fig. 4.8. The amplifier was simulated using Keysight Advanced Design System (ADS) and measured with Copper Mountain Planar TR1300/1 and Agilent N5225A.

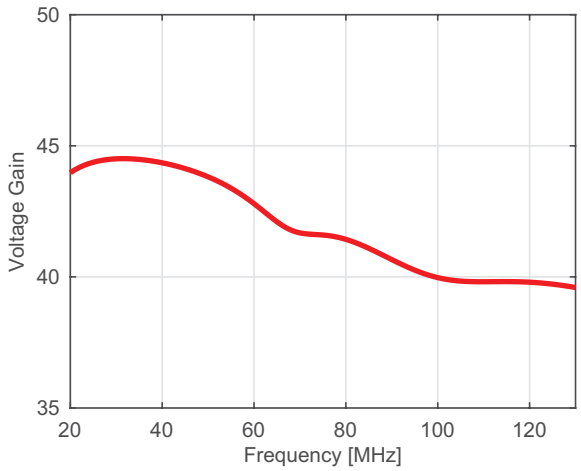

Figure 4.8 The voltage gain of the common-base amplifier.

4.1.3.3 Matching Network Design Using a Transformer and a Negative Impedance Converter

The matching part of the proposed circuit consists of a transformer and a BJT-NIC. The transformer is used to match the input resistance of the common-base amplifier and that of the electrically-small monopole antenna. The transformer used in the proposed circuit is a Mini-Circuits Surface Mount RF Transformer, T14-1-KK81. This transformer can operate from 0.2 MHz to 150 MHz, and its turns ratio is $14 : 1$. The purpose of using this transformer as the second stage circuit is to convert the input resistance of the common-base amplifier and the antenna to $50\ \Omega$. Placing the common-base amplifier and transformer before the NIC circuit contributes to the system stability because the NIC is now connected to a load having a real part of $50\ \Omega$ and a small reactance instead of the high Q monopole antenna, which has a small resistance and high reactance. In other words, the reflection coefficient that the NIC sees towards the load is now decreased. The Simulated and measured magnitudes of the input impedance of the transformer are shown in Fig. 4.9. The transformer was simulated in ADS using the model file provided by Mini-Circuits. The measurement was carried out using Agilent N5225A network analyzer. As can be observed, the simulation and measurement results are generally in good agreement. However, minor differences exist between the measured results and the results obtained by the simulation using the model provided by the vendor. Note that the magnitude of the input impedance of an ideal 14:1 transformer is $700\ \Omega$ ($50\ \Omega \times 14$).

To match the input reactance of the transformer, the common-base amplifier, and the antenna, a BJT-NIC is designed. The architecture of this BJT-NIC is based on a Linvill's floating NIC [45], which is composed of two transistors, dc bias circuits, RF chokes and dc blocks, as shown in 4.6(b). The bias circuits, the RF chokes ($L_c = 2.7\ \mu$H) and two of the four DC blocks ($C_{d1} = 47$ nF) used in our BJT-NIC are the same as those

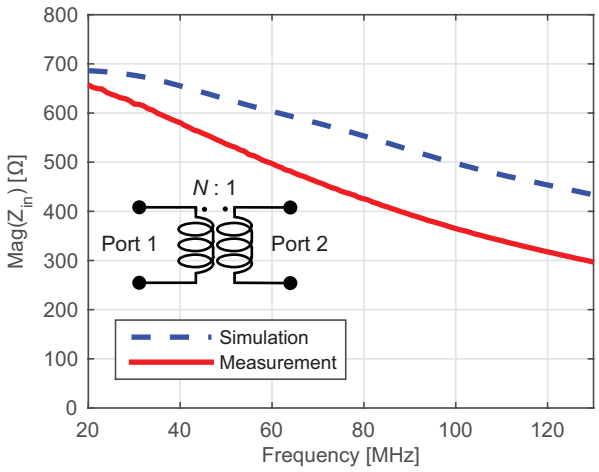

Figure 4.9 The magnitude of the input impedance of the transformer.

used in our common-base amplifier. The two DC blocks functioning in the feedback loop of the proposed BJT-NIC ($C_{d2} = 10$ pF) have different values from those used in the amplifier circuit. This is because the stability of the NIC is determined by the gain of the feedback loop, which can be controlled by these two capacitors. Specifically, these capacitors (C_{d2}) not only act as DC blocks, but also as tuning elements for the feedback loop gain and the system stability. The proposed BJT-NIC is a symmetrical circuit, and the circuit layout is also symmetrical. The detailed schematic of the proposed BJT-NIC is shown in Fig. 4.6(b). The ports of BJT-NIC are defined in Fig. 4.10(a), and the simulated and measured reflection coefficients (S_{11}) and transmission coefficients (S_{21}) of the BJT-NIC are shown in Figs. 4.10(b) and (c), respectively. The measured S_{11} remains below -9.5 dB, and the measured S_{21} varies from -4.4 dB to -7.5 dB over the examined frequency band (20 MHz–130 MHz). The simulated and measured input reactances of the BJT-NIC are shown in Fig. 4.10(d). As can be observed, the BJT-NIC has a negative slope of frequency response which is equivalent to a negative inductor or a non-Foster element. The simulations were done using ADS. The measurements were carried out using Copper Mountain Planar TR1300/1 and Agilent N5225A.

4.1.4 Stability Analysis and System Performance

4.1.4.1 Stability Analysis

Figs. 4.6 (a) and (b) show the simplified and the complete schematics of the non-Foster transmitting system. To examine the stability of the system, a stability analysis was performed. This analysis requires the antenna model to be a two-port network as shown in Figs. 4.3 and 4.6 (a). To do this, the proposed antenna is first simulated in FEKO and its scattering parameters were obtained. The one-port scattering matrix of the antenna is then converted to a two-port scattering matrix where the second port is a radiation port,

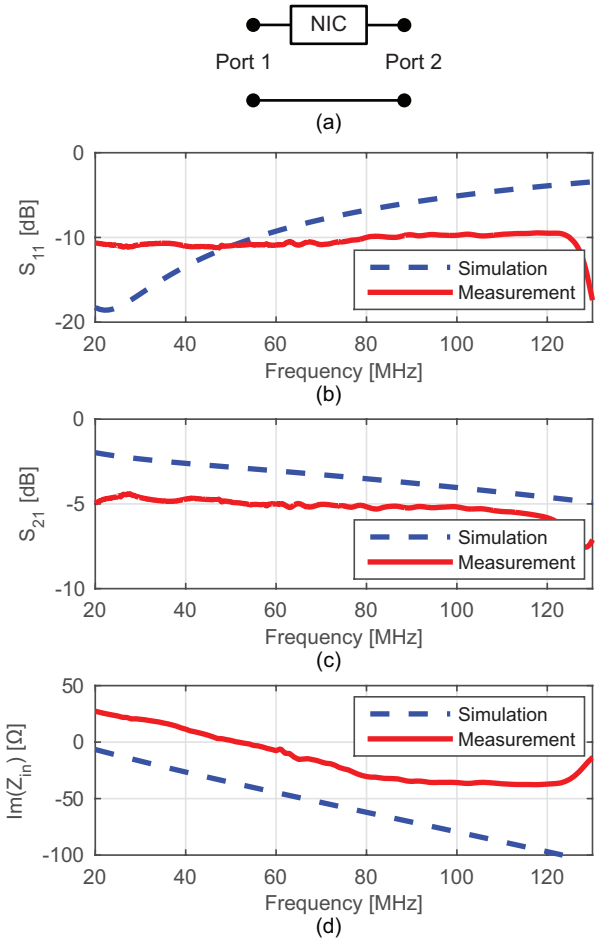

Figure 4.10 (a) The port definition of the NIC. (b) The S_{11}, (c) S_{21}, and (d) the imaginary part of the input impedance of the NIC.

following the method discussed in [97]. The stability analysis of the system consisting of the antenna, the common-based amplifier, the transformer and the BJT-NIC was done in the circuit-based simulator, Keysight ADS. The stability factors μ and μ' are given by [98]:

$$\mu = \frac{1 - |S_{11}|^2}{|S_{22} - \Delta S_{11}^*| + |S_{12}S_{21}|} \tag{4.14}$$

$$\mu' = \frac{1 - |S_{22}|^2}{|S_{11} - \Delta S_{22}^*| + |S_{12}S_{21}|}. \tag{4.15}$$

The value of the stability factors μ (μ') gives the distance from the center of the Smith chart to the nearest unstable load (source) impedance values. If $\mu > 1$ ($\mu' > 1$) in the system simulation, the system is unconditionally stable. The simulated stability factors of the non-Foster transmitting system are shown in Figs. 4.11(a) and (b). As can be observed, the proposed system is unconditionally stable ($\mu > 1$ and $\mu' > 1$). Note that the method used for calculating stability factors requires the antenna to be modeled as a two-port network. However, when doing the measurements for the transmitting system, the electrically-small monopole antenna is a 1-port device. Hence, it is not practical to examine the measured system stability using this method.

4.1.4.2 System Performance

To analyze the performance of the proposed non-Foster matching network, prototypes of the complete proposed circuit and the antenna were fabricated, as shown in Figs. 4.12 and 4.13. The circuit was fabricated on a FR4 substrate ($\epsilon_r = 4.4$, thickness $= 0.063$", $tan\delta = 0.02$) using standard printed circuit board (PCB) fabrication technologies. The complete list of the bill of materials of the components is presented in Table 4.1. The electrically-small monopole antenna was realized using a brass rod (height $= 12$", Diameter $= 0.5$"). It is fed by a SMA connector (feed height $= 0.59$"), and placed on

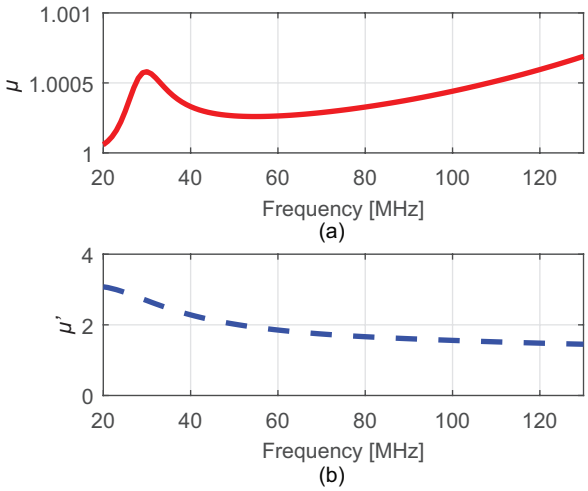

Figure 4.11 The simulated stability factors of the non-Foster transmitting system: (a) μ and (b) μ'.

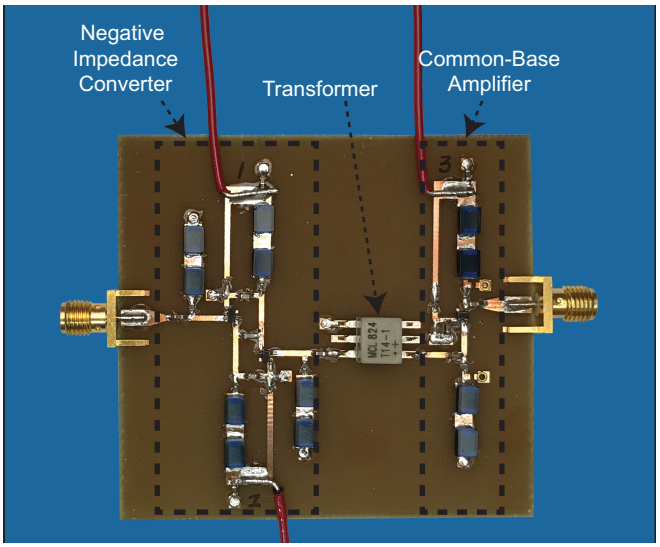

Figure 4.12 Prototype of the non-Foster transmit matching circuit.

a brass sheet (12" $\times$ 12" $\times$ 0.016"). Styrofoam material is used to support the monopole rod as shown in Fig. 4.13. The antenna connected with the non-Foster matching circuit is shown in Fig. 4.13.

The simulated and measured S_{11}, S_{21}, and S_{21} improvement are shown in Figs. 4.14, 4.15, and 4.16, respectively. The system simulation was conducted in Keysight ADS. The measurement was done using a portable Vector Network Analyzer (VNA), Copper Mountain Planar TR1300/1, and power supplies. Fig. 4.15 shows the transducer gain of the isolated electrically-small monopole, the antenna matched with a NIC matching circuit (the same architecture as the NIC used in our circuit), and the antenna matched with the proposed non-Foster matching circuit are simulated in ADS. Compared to the isolated antenna, the S_{21} of the NIC matched antenna is enhanced but by only a very small value in the lower frequency band. This is expected since the intrinsic loss of the NIC is magnified as discussed in Section 4.1.2.2. In contrast, using the proposed matching network, the system attains high S_{21} throughout the examined frequency band (20 MHz–130 MHz).

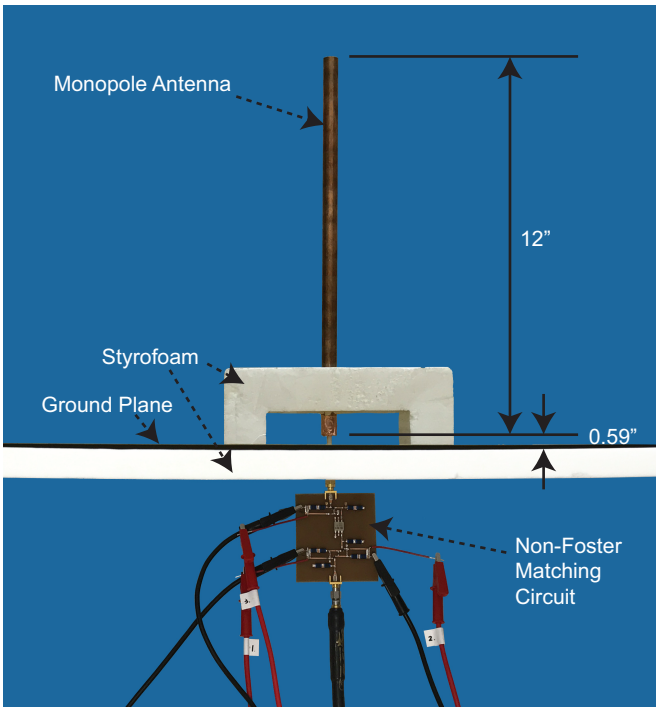

Figure 4.13 Prototype of the non-Foster transmitting system.

Table 4.1 The bill of material of the components for the non-Foster transmit matching circuit.

Component	Model/Value	Component	Model/Value
BJT	BFP540ESD	R_{b2}	1.33 kΩ
C_{d1}	47000 pF	R_c	196 Ω
C_{d2}	10 pF	R_e	237 Ω
C_b	47000 pF	L_{load}	150 nH
R_{b1}	1.1 kΩ	L_c	2.7 μH

Note that the values of S_{21} in dB scale are equal to those of the transducer power gain (transmission efficiency) in dB scale. Since measuring exact values of S_{21} requires the antenna to be a two-port network, which is not the case in real antenna prototypes, the contribution of the proposed circuit to the transmission efficiency is evaluated by measuring the improvement of S_{21}. In the measurement setup, port 1 and port 2 of the VNA were connected to the proposed transmitting system and a receiving antenna, respectively. In the SOLT (Short-Open-Load-Through) calibration procedure, "through" was defined as the transmission coefficient between the transmitting antenna without the proposed matching network and the receiving antenna. Therefore, in this measurement, the transmission coefficients between the proposed transmitting system and the receiving antenna directly represent the S_{21} improvement (i.e. the difference between the transmitting system with and without the proposed circuit). Fig. 4.16 shows the simulated and measured S_{21} improvement. Observe that the transmitting system with the proposed non-Foster matching circuit has a 34.4 dB higher S_{21} compared to the same system without the circuit, as can be observed in Fig. 4.16. The 6 dB return loss bandwidth of the system is measured to be 110%, (Fig. 4.14) and the system also remains stable within the frequency band of operation (26 MHz–89 MHz). Significant ripples can be observed from 88 MHz to 108 MHz in Fig. 4.16. This is because the measurements were not performed in an anechoic chamber [4], and other operating wireless communication systems, especially FM radios, have interfered our measurements.

[4]Due to the large wavelengths in the frequency band of interest, it is not practical to conduct the measurements in our anechoic chamber.

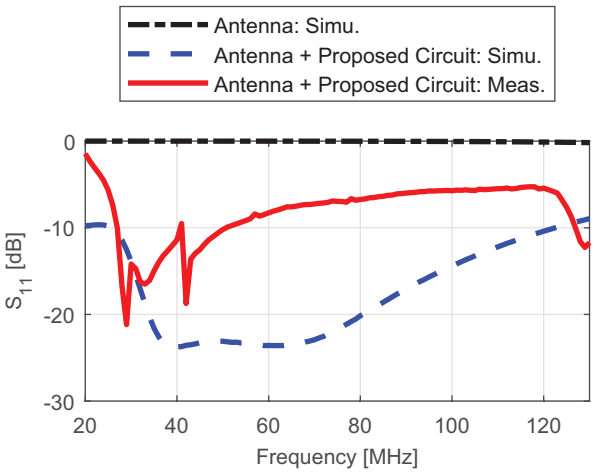

Figure 4.14 The simulated S_{11} of the electrically-small monopole antenna in isolation and the simulated and measured S_{11} of the non-Foster transmitting system.

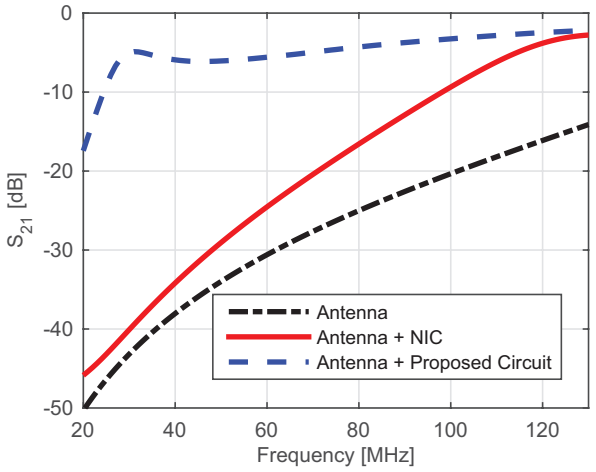

Figure 4.15 The simulated S_{21} of the electrically-small monopole antenna in isolation, with the NIC, and with the proposed non-Foster transmit matching circuit.

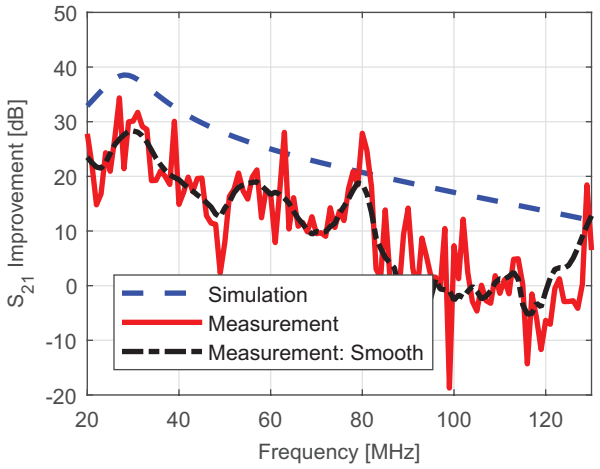

Figure 4.16 The simulated and measured S_{21} improvement of the non-Foster transmitting system.

4.1.5 Conclusions

The results presented in this paper show that the proposed non-Foster matching architecture allows electrically-small antennas (ESAs) for transmit applications simultaneously achieve wide bandwidth, stability, and high transmission efficiency (transducer power gain). The design concepts and details of the new non-Foster matching circuit were discussed using an example where the electrically-small monopole antenna functions in a transmit application in the HF/VHF frequency bands. In the example examined in this paper, the 12" high brass monopole ESA with a 0.5" diameter is placed on a 24"$\times$24" brass ground plane and probe-fed with a SMA connector. A common-base amplifier is employed as the first stage of the proposed non-Foster transmit matching circuit. This common-base amplifier is not only designed to generate the voltage necessary for power transmission, but also to provide a 4.6 dB–5.7 dB gain and a 45.6 dB–66.3 dB isolation between the matching circuit and the ESA in order to reduce the multiple reflections that magnify mismatch losses and result in low transmission efficiency (transducer power gain). The second stage of the proposed non-Foster matching architecture is a commercial off-the-shelf transformer with a $14:1$ turns ratio. Using this transformer, the input resistance of the common-base amplifier and the antenna are matched to 50Ω. This brings the benefit of stability improvement. Following the transformer, a symmetrical Bipolar-junction-transistor-based negative impedance converter is designed to create negative inductance in order to match the reactance of the transformer, common-base amplifier, and the antenna. A measured 110% 6 dB return loss fractional bandwidth is achieved by the proposed transmitting system. When the same ESA is matched with conventional passive matching circuits (Foster circuits), the maximum available bandwidth is 0.076%. The improvement of the transmission efficiency of the system is measured to be as much as 34.4 dB compared to the same antenna without the proposed circuit. The system also remains

stable throughout the entire operating frequency band (26 MHz–89 MHz). The design concepts and the topology of the proposed non-Foster transmit matching architecture are equally applicable to other electrically-small transmitting system.

Chapter 5

Future Work

In the previous chapters, I investigated bandwidth enhancement and miniaturization techniques for small antennas: improving the antenna structure, utilizing the platform, and using non-Foster matching circuits. The immediate future work based on this dissertation is to develop a non-Foster platform-mounted antenna.

As discussed in Chapter 3, antennas mounted on a large platform can be used as inductive or capacitive coupling elements that excite desired characteristic modes of the platform. In the example presented in Chapter 3, the impedance bandwidth of the platform-mounted antenna functioning in the high-frequency (HF) band was successfully enhanced as much as 10 times. However, for applications that function in the lower part of the HF band or even lower frequencies, most antennas are extremely electrically-small due to the extremely large wavelength in these frequencies (e.g. 100 m at 3 MHz) and have very limited bandwidth (e.g. $\ll 24$kHz). In such cases, even with a ten-time enhancement, the bandwidth may not be wide enough for applications that seek higher data rate. Fortunately, the non-Foster matching circuit presented in Chapter 4 can be used to bypass the gain-bandwidth limitation of antennas. The combination of these two bandwidth enhancement methods has great potential to allow antenna systems working in the lower frequencies achieve exceptionally wide impedance bandwidth. Specifically, the coupling elements used to excite platform modes can be designed to possess non-Foster characteristics. By doing so, the advantage of two bandwidth enhancement methods can be combined. In addition, the utilization of the platform (instead of the antennas) as the main radiator decreases the quality factor of the system. In other words, the input resistance of the system increases and the reactance of the system decreases. This alleviates some challenging problems (e.g. the need for a high turns ratio transformer and the requirement for a high voltage swing at the antenna terminal) in non-Foster circuit design, making the integration of these two techniques even more advantageous.

LIST OF REFERENCES

[1] H. Wheeler, "Fundamental limitations of small antennas," *Proc. IRE*, vol. 35, no. 12, pp. 1479–1484, Dec. 1947.

[2] L. J. Chu, "Physical limitations of omni-directional antennas," *J. Applied Physics*, vol. 19, no. 12, pp. 1163–1175, Dec. 1948.

[3] R. Harrington, "On the gain and beamwidth of directional antennas," *IRE Transactions on Antennas and Propagation*, vol. 6, no. 3, pp. 219–225, Jul. 1958.

[4] ——, "Antenna excitation for maximum gain," *IEEE Transactions on Antennas and Propagation*, vol. 13, no. 6, pp. 896–903, Nov. 1965.

[5] R. Hansen, "Fundamental limitations in antennas," *Proceedings of the IEEE*, vol. 69, no. 2, pp. 170–182, Feb. 1981.

[6] R. Fante, "Maximum possible gain for an arbitrary ideal antenna with specified quality factor," *IEEE Transactions on Antennas and Propagation*, vol. 40, no. 12, pp. 1586–1588, Dec. 1992.

[7] J. McLean, "A re-examination of the fundamental limits on the radiation Q of electrically small antennas," *IEEE Trans. Antennas Propag.*, vol. 44, no. 5, pp. 672–676, May 1996.

[8] J. Thal, H.L., "Gain and Q Bounds for Coupled TM-TE Modes," *IEEE Transactions on Antennas and Propagation*, vol. 57, no. 7, pp. 1879–1885, Jul. 2009.

[9] R. E. Collin, "Minimum Q of small antennas," *Journal of Electromagnetic Waves and Applications*, vol. 12, no. 10, pp. 1369–1393, Jan. 1998. [Online]. Available: http://dx.doi.org/10.1163/156939398X01457

[10] H. Thal, "New radiation limits for spherical wire antennas," *IEEE Trans. Antennas Propag.*, vol. 54, no. 10, pp. 2757–2763, Oct. 2006.

[11] M. Gustafsson, M. Cismasu, and B. L. G. Jonsson, "Physical Bounds and Optimal Currents on Antennas," *IEEE Transactions on Antennas and Propagation*, vol. 60, no. 6, pp. 2672–2681, Jun. 2012.

[12] S. A. Schelkunoff, "A Mathematical Theory of Linear Arrays," *Bell System Technical Journal*, vol. 22, no. 1, pp. 80–107, Jan. 1943. [Online]. Available: http://onlinelibrary.wiley.com/doi/10.1002/j.1538-7305.1943.tb01306.x/abstract

[13] C. Dolph, "A Current Distribution for Broadside Arrays Which Optimizes the Relationship between Beam Width and Side-Lobe Level," *Proceedings of the IRE*, vol. 34, no. 6, pp. 335–348, Jun. 1946.

[14] P. Woodward and J. Lawson, "The Theoretical Precision with which an Arbitrary Radiation-Pattern may be Obtained from a Source of Finite Size," *Journal of the Institution of Electrical Engineers - Part III: Radio and Communication Engineering*, vol. 95, no. 37, pp. 363–370, Sep. 1948.

[15] D. Tucker, "Superdirective arrays: the use of decoupling between elements to ease design and increase bandwidth," *Radio and Electronic Engineer*, vol. 34, no. 4, pp. 251–256, Oct. 1967.

[16] G. Walker, C. Haden, and O. Ramer, "Superconducting superdirectional antenna arrays," *IEEE Transactions on Antennas and Propagation*, vol. 25, no. 6, pp. 885–887, Nov. 1977.

[17] M. Gustafsson and S. Nordebo, "Optimal Antenna Currents for Q, Superdirectivity, and Radiation Patterns Using Convex Optimization," *IEEE Transactions on Antennas and Propagation*, vol. 61, no. 3, pp. 1109–1118, 2013.

[18] F. E. Terman, *Radio engineers' handbook*. New York; London: McGraw-Hill Book Co., 1943.

[19] A. Yaghjian and S. Best, "Impedance, bandwidth, and Q of antennas," *IEEE Trans. Antennas Propag.*, vol. 53, no. 4, pp. 1298–1324, Apr. 2005.

[20] J. L. Volakis, C.-C. Chen, and K. Fujimoto, *Small antennas: miniaturization techniques & applications*. New York: McGraw-Hill, 2010.

[21] H. W. Bode, *Network Analysis and Feedback Amplifier Design*. [S.l.]: Van Nostrand, 1947.

[22] R. M. Fano, "Theoretical limitations on the broadband matching of arbitrary impedances," *Journal of the Franklin Institute*, vol. 249, no. 1, pp. 57–83, Jan. 1950. [Online]. Available: http://www.sciencedirect.com/science/article/pii/0016003250900068

[23] D. Youla, "A New Theory of Broad-band Matching," *IEEE Transactions on Circuit Theory*, vol. 11, no. 1, pp. 30–50, Mar. 1964.

[24] H. Nakano and J. Yamauchi, "Characteristics of modified spiral and helical antennas," *IEE Proc. Part H*, vol. 129, no. 5, pp. 232–237, Oct. 1982.

[25] E. T. Roland and W. F. Patterson, "A Slow-Wave Flat Spiral Antenna," in *17th USAF Antenna Symposium (U. of Illinois, Allerton)*, vol. 111, Nov. 1967.

[26] D. Filipovic and J. Volakis, "Broadband meanderline slot spiral antenna," *IEE Proc. Microwaves Antennas Propag.*, vol. 149, no. 2, pp. 98–105, Apr. 2002.

[27] B. Kramer, M. Lee, C.-C. Chen, and J. Volakis, "Miniature UWB Antenna with Embedded Inductive Loading," in *2006 IEEE International Workshop on Antenna Technology Small Antennas and Novel Metamaterials*, Mar. 2006, pp. 289–292.

[28] M. Lee, B. Kramer, C.-C. Chen, and J. Volakis, "Distributed Lumped Loads and Lossy Transmission Line Model for Wideband Spiral Antenna Miniaturization and Characterization," *IEEE Trans. Antennas Propag.*, vol. 55, no. 10, pp. 2671–2678, Oct. 2007.

[29] B. Kramer, C. Chen, and J. Volakis, "Size Reduction of a Low-Profile Spiral Antenna Using Inductive and Dielectric Loading," *IEEE Antennas Wireless Propag. Lett.*, vol. 7, pp. 22–25, 2008.

[30] B. Kramer, C.-C. Chen, M. Lee, and J. Volakis, "Fundamental Limits and Design Guidelines for Miniaturizing Ultra-Wideband Antennas," *IEEE Antennas Propag. Mag.*, vol. 51, no. 4, pp. 57–69, Aug. 2009.

[31] S. Best, "On the use of scale brass models in HF shipboard communication antenna design," *IEEE Antennas Propag. Mag.*, vol. 44, no. 2, pp. 12–23, Apr. 2002.

[32] J. Chalas, K. Sertel, and J. Volakis, "NVIS synthesis for electrically small aircraft using characteristic modes," in *2014 IEEE Antennas and Propagation Society International Symposium (APSURSI)*, Jul. 2014, pp. 1431–1432.

[33] M. Ignatenko and D. Filipovic, "Application of characteristic mode analysis to HF low profile vehicular antennas," in *2014 IEEE Antennas and Propagation Society International Symposium (APSURSI)*, Jul. 2014, pp. 850–851.

[34] G. Marrocco, L. Mattioni, and V. Martorelli, "Naval structural antenna systems for broadband HF communications–Part II: Design methodology for real naval platforms," *IEEE Trans. Antennas Propag.*, vol. 54, no. 11, pp. 3330–3337, Nov. 2006.

[35] G. Marrocco and L. Mattioni, "Naval structural antenna systems for broadband HF communications," *IEEE Trans. Antennas Propag.*, vol. 54, no. 4, pp. 1065–1073, Apr. 2006.

[36] L. Mattioni, D. Di Lanzo, and G. Marrocco, "Naval structural antenna systems for broadband HF communications–Part III: Experimental evaluation on scaled prototypes," *IEEE Trans. Antennas Propag.*, vol. 56, no. 7, pp. 1882–1887, Jul. 2008.

[37] M. Koubeissi, B. Pomie, and E. Rochefort, "Perspectives of HF half loop antennas for stealth combat ships," *Prog. Electromagn. Res. B*, vol. 54, pp. 167–184, 2013. [Online]. Available: http://www.jpier.org/PIERB/pier.php?paper=13050201

[38] Y. Chen and C.-F. Wang, "HF band shipboard antenna design using characteristic modes," *IEEE Trans. Antennas Propag.*, vol. 63, no. 3, pp. 1004–1013, Mar. 2015.

[39] ——, "Electrically small UAV antenna design using characteristic modes," *IEEE Trans. Antennas Propag.*, vol. 62, no. 2, pp. 535–545, Feb. 2014.

[40] A. D. Harris and G. A. Myers, "An investigation of broadband miniature antennas," Naval Postgraduate School, Tech. Rep., Sep. 1968.

[41] A. K. Perry, "Broadband Antenna Systems Realized from Active Circuit Conjugate Impedance Matching," Master's thesis, Naval Postgraduate School, Monterey, CA, Sep. 1973.

[42] A. Bahr, "On the use of active coupling networks with electrically small receiving antennas," *IEEE Trans. Antennas Propag.*, vol. 25, no. 6, pp. 841–845, Nov. 1977.

[43] S. Sussman-Fort and R. Rudish, "Non-Foster Impedance Matching of Electrically-Small Antennas," *IEEE Trans. Antennas Propag.*, vol. 57, no. 8, pp. 2230–2241, Aug. 2009.

[44] M. M. Jacob and D. F. Sievenpiper, "Gain and Noise Analysis of Non-Foster Matched Antennas," *IEEE Transactions on Antennas and Propagation*, vol. 64, no. 12, pp. 4993–5004, Dec. 2016.

[45] J. Linvill, "Transistor Negative-Impedance Converters," *Proceedings of the IRE*, vol. 41, no. 6, pp. 725–729, Jun. 1953.

[46] S. E. Sussman-Fort and R. M. Rudish, "Non-Foster Impedance Matching for Transmit Applications," in *IEEE International Workshop on Antenna Technology Small Antennas and Novel Metamaterials, 2006.*, Mar. 2006, pp. 53–56.

[47] R. C. Hansen and R. E. Collin, *Small antenna handbook*. Hoboken, N.J.: John Wiley & Sons, 2011.

[48] E. Ugarte-Munoz, S. Hrabar, D. Segovia-Vargas, and A. Kiricenko, "Stability of Non-Foster Reactive Elements for Use in Active Metamaterials and Antennas," *IEEE Transactions on Antennas and Propagation*, vol. 60, no. 7, pp. 3490–3494, Jul. 2012.

[49] N. Behdad and K. Sarabandi, "A compact dual-/multi-band wireless LAN antenna," in *2005 IEEE Antennas and Propagation Society International Symposium*, vol. 2B, 2005, pp. 527–530.

[50] ——, "Wideband double-element ring slot antenna," *Electron. Lett.*, vol. 40, no. 7, pp. 408–409, 2004.

[51] J. Kaiser, "The Archimedean two-wire spiral antenna," *IRE Trans. Antennas Propag.*, vol. 8, no. 3, pp. 312 –323, May 1960.

[52] Z. Wang, S. Fang, S. Fu, and S. Jia, "Single-Fed Broadband Circularly Polarized Stacked Patch Antenna With Horizontally Meandered Strip for Universal UHF RFID Applications," *IEEE Trans. Microw. Theory Techn.*, vol. 59, no. 4, pp. 1066–1073, Apr. 2011.

[53] J. Pourahmadazar and V. Rafii, "Broadband circularly polarised slot antenna array for L- and S-band applications," *Electron. Lett.*, vol. 48, no. 10, pp. 542–543, May 2012.

[54] X. Chen and Wiley InterScience (Online service), *Antennas for global navigation satellite systems*. Chichester, West Sussex, U.K.; Hoboken, N.J.: John Wiley & Sons, 2012. [Online]. Available: http://dx.doi.org/10.1002/9781119969518

[55] J. Wang, "Antennas for Global Navigation Satellite System (GNSS)," *Proc. IEEE*, vol. 100, no. 7, pp. 2349–2355, Jul. 2012.

[56] Y. Yao, X. Wang, X. Chen, J. Yu, and S. Liu, "Novel Diversity/MIMO PIFA Antenna With Broadband Circular Polarization for Multimode Satellite Navigation," *IEEE Antennas Wireless Propag. Lett.*, vol. 11, pp. 65–68, 2012.

[57] S. Gao, Y. Qin, and A. Sambell, "Low-Cost Broadband Circularly Polarized Printed Antennas and Array," *IEEE Antennas Propag. Mag.*, vol. 49, no. 4, pp. 57–64, Aug. 2007.

[58] Y.-X. Guo, L. Bian, and X. Q. Shi, "Broadband Circularly Polarized Annular-Ring Microstrip Antenna," *IEEE Trans. Antennas Propag.*, vol. 57, no. 8, pp. 2474–2477, Aug. 2009.

[59] J.-H. Lu and S.-F. Wang, "Planar Broadband Circularly Polarized Antenna With Square Slot for UHF RFID Reader," *IEEE Trans. Antennas Propag.*, vol. 61, no. 1, pp. 45–53, Jan. 2013.

[60] X. Quan, R. Li, and M. Tentzeris, "A Broadband Omnidirectional Circularly Polarized Antenna," *IEEE Trans. Antennas Propag.*, vol. 61, no. 5, pp. 2363–2370, May 2013.

[61] J. Bell and M. Iskander, "A low-profile Archimedean spiral antenna using an EBG ground plane," *IEEE Antennas Wireless Propag. Lett.*, vol. 3, no. 1, pp. 223–226, 2004.

[62] T. Iwasaki, A. P. Freundorfer, and K. Iizuka, "A unidirectional semi-circle spiral antenna for subsurface radars," *IEEE Trans. Electromagn. Compat.*, vol. 36, no. 1, pp. 1–6, Feb. 1994.

[63] J. Volakis, M. Nurnberger, and D. Filipovic, "A broadband cavity-backed slot spiral antenna," *IEEE Antennas Propag. Mag.*, vol. 43, no. 6, pp. 15–26, 2001.

[64] W. Cao, A. Liu, B. Zhang, T. Yu, and Z. Qian, "Dual-Band Spiral Patch-Slot Antenna With Omnidirectional CP and Unidirectional CP Properties," *IEEE Trans. Antennas Propag.*, vol. 61, no. 4, pp. 2286–2289, Apr. 2013.

[65] H. Nakano, S. Sasaki, H. Oyanagi, and J. Yamauchi, "Cavity-backed Archimedean spiral antenna with strip absorber," *IET Microw. Antennas Propag.*, vol. 2, no. 7, pp. 725–730, 2008.

[66] Q. Li and Z. Shen, "An inverted microstrip-fed cavity-backed slot antenna for circular polarization," *IEEE Antennas Wireless Propag. Lett.*, vol. 1, no. 1, pp. 190–192, 2002.

[67] A. Bhobe and D. Filipovic, "Cavity backed four-arm slot like spiral antenna for dual mode operation," in *IEEE Antennas and Propagation Society International Symposium, 2003*, vol. 2, 2003, pp. 165–168 vol.2.

[68] D. Psychoudakis, J. Volakis, Z. Wing, and J. W. Halloran, "Cavity-Backed Miniature Wideband UHF Circular Polarized Antenna With Textured Dielectrics," *IEEE Trans. Antennas Propag.*, vol. 54, no. 12, pp. 3586–3592, 2006.

[69] R. Li, B. Pan, A. Traille, J. Papapolymerou, J. Laskar, and M. Tentzeris, "Development of a Cavity-Backed Broadband Circularly Polarized Slot/Strip Loop Antenna With a Simple Feeding Structure," *IEEE Trans. Antennas Propag.*, vol. 56, no. 2, pp. 312–318, 2008.

[70] H. Nakano, T. Igarashi, H. Oyanagi, Y. Iitsuka, and J. Yamauchi, "Unbalanced-Mode Spiral Antenna Backed by an Extremely Shallow Cavity," *IEEE Trans. Antennas Propag.*, vol. 57, no. 6, pp. 1625–1633, 2009.

[71] K.-F. Hung and Y.-C. Lin, "Novel Broadband Circularly Polarized Cavity-Backed Aperture Antenna With Traveling Wave Excitation," *IEEE Trans. Antennas Propag.*, vol. 58, no. 1, pp. 35–42, 2010.

[72] Q. C. Zhang and W. Wu, "Compact dual-band circularly-polarised cavity-backed slot antenna," *Electron. Lett.*, vol. 47, no. 17, pp. 947–948, 2011.

[73] Y.-J. Hu, W.-P. Ding, W.-M. Ni, and W.-Q. Cao, "Broadband Circularly Polarized Cavity-Backed Slot Antenna Array With Four Linearly Polarized Disks Located in a Single Circular Slot," *IEEE Antennas Wireless Propag. Lett.*, vol. 11, pp. 496–499, 2012.

[74] N. Behdad and M. Al-Joumayly, "A Generalized Synthesis Procedure for Low-Profile, Frequency Selective Surfaces With Odd-Order Bandpass Responses," *IEEE Trans. Antennas Propag.*, vol. 58, no. 7, pp. 2460–2464, 2010.

[75] N. Behdad, "A second-order band-pass frequency selective surface using nonresonant subwavelength periodic structures," *Microw. Opt. Technol. Lett.*, vol. 50, no. 6, pp. 1639–1643, 2008.

[76] P. J. Baldwin, A. Boswell, D. Brewster, and J. Allwright, "Iterative calculation of ship-borne HF antenna performance," *IEE Proc. Part H Microwaves Antennas Propag.*, vol. 138, no. 2, pp. 151–158, Apr. 1991.

[77] A. Spezio, "Electronic warfare systems," *IEEE Trans. Microw. Theory Techn.*, vol. 50, no. 3, pp. 633–644, Mar. 2002.

[78] B. Austin and K. Murray, "The application of characteristic-mode techniques to vehicle-mounted NVIS antennas," *IEEE Antennas Propag. Mag.*, vol. 40, no. 1, pp. 7–21, 30, Feb. 1998.

[79] R. Ziolkowski, "An efficient, electrically small antenna designed for VHF and UHF applications," *IEEE Antennas Wireless Propag. Lett.*, vol. 7, pp. 217–220, 2008.

[80] H. Li, Y. Tan, B. K. Lau, Z. Ying, and S. He, "Characteristic mode based tradeoff analysis of antenna-chassis interactions for multiple antenna terminals," *IEEE Trans. Antennas Propag.*, vol. 60, no. 2, pp. 490–502, Feb. 2012.

[81] Z. Miers, H. Li, and B. K. Lau, "Design of bandwidth-enhanced and multiband MIMO antennas using characteristic modes," *IEEE Antennas Wireless Propag. Lett.*, vol. 12, pp. 1696–1699, 2013.

[82] K. K. Kishor and S. V. Hum, "A two-port chassis-mode MIMO antenna," *IEEE Antennas Wireless Propag. Lett.*, vol. 12, pp. 690–693, 2013.

[83] ——, "A pattern reconfigurable chassis-mode MIMO antenna," *IEEE Trans. Antennas Propag.*, vol. 62, no. 6, pp. 3290–3298, Jun. 2014.

[84] T.-Y. Shih and N. Behdad, "Design of platform-mounted HF/VHF antennas using the characteristic modes theory," in *2015 International Workshop on Antenna Technology (iWAT)*, Mar. 2015, pp. 84–86.

[85] ——, "Bandwidth enhancement of HF antennas mounted on military platforms using a Characteristic-Modes-Based Design Approach," in *2015 International Symposium on Antennas and Propagation (ISAP)*, Nov. 2015, pp. 1–3.

[86] ——, "Bandwidth enhancement of platform-mounted HF antennas using the characteristic modes theory," in *2015 IEEE International Symposium on Antennas and Propagation USNC/URSI National Radio Science Meeting*, Jul. 2015, pp. 1608–1609.

[87] "Expeditionary fighting vehicle," Oct. 2014, page Version ID: 621202886. [Online]. Available: http://en.wikipedia.org/wiki/Expeditionary_Fighting_Vehicle

[88] R. Garbacz, "Modal expansions for resonance scattering phenomena," *Proc. IEEE*, vol. 53, no. 8, pp. 856–864, Aug. 1965.

[89] R. Garbacz and R. Turpin, "A generalized expansion for radiated and scattered fields," *IEEE Trans. Antennas Propag.*, vol. 19, no. 3, pp. 348–358, May 1971.

[90] R. F. Harrington and J. Mautz, "Computation of characteristic modes for conducting bodies," *IEEE Trans. Antennas Propag.*, vol. 19, no. 5, pp. 629–639, Sep. 1971.

[91] ——, "Theory of characteristic modes for conducting bodies," *IEEE Trans. Antennas Propag.*, vol. 19, no. 5, pp. 622–628, Sep. 1971.

[92] M. Cabedo-Fabres, E. Antonino-Daviu, A. Valero-Nogueira, and M. Bataller, "The theory of characteristic modes revisited: A contribution to the design of antennas for modern applications," *IEEE Antennas Propag. Mag.*, vol. 49, no. 5, pp. 52–68, Oct. 2007.

[93] W. Geyi, "A method for the evaluation of small antenna Q," *IEEE Trans. Antennas Propag.*, vol. 51, no. 8, pp. 2124–2129, Aug. 2003.

[94] K. Ghaemi and N. Behdad, "A Low-Profile, Vertically Polarized Ultrawideband Antenna With Monopole-Like Radiation Characteristics," *IEEE Trans. Antennas Propag.*, vol. 63, no. 8, pp. 3699–3705, Aug. 2015.

[95] T.-Y. Shih and N. Behdad, "Bandwidth enhancement of platform-mounted HF antennas using the characteristic mode theory," *IEEE Trans. Antennas Propag.*, vol. 64, no. 7, pp. 2648–2659, Jul. 2016.

[96] G. Gonzalez, *Microwave transistor amplifiers: analysis and design*. Upper Saddle River, N.J.: Prentice Hall, 1997.

[97] J. Aberle, "Two-Port Representation of an Antenna With Application to Non-Foster Matching Networks," *IEEE Trans. Antennas Propag.*, vol. 56, no. 5, pp. 1218–1222, May 2008.

[98] M. Edwards and J. Sinsky, "A new criterion for linear 2-port stability using a single geometrically derived parameter," *IEEE Transactions on Microwave Theory and Techniques*, vol. 40, no. 12, pp. 2303–2311, Dec. 1992.